Parameters Variation and Flow Characteristics when CO_2 Displacing Brine in Four Micromodels Simulating Carbon Sequestration in Saline Aquifers

Changzhong Zhao[1], Yi Zhang[1*], Ke Chen[1], Lei Yuan[1], Shezhan Liu[1], Mingkun Chen[1], Yongchen Song[1]

[1]Key Laboratory of Ocean Energy Utilization and Energy Conservation of Ministry of Education, School of Energy and Power Engineering, Dalian University of Technology, Dalian 116024, China.

Key Points:

- Structure, flow rate and salinity all affected the amount and safety of CO_2 captured during the sequestration in saline aquifers
- The displacement pattern was not constant during the flow through theoretical analysis and experimental result of velocity and force field
- Back flow, corner flow and more intense Haines jump were found when CO_2 displaced brine in different displacement patterns.

Abstract

Two-phase flow of CO_2/brine in porous media is critical to the capacity and safety of carbon sequestration into the brine aquifer. In order to provide valuable information and important theoretical basis for site selection and CO_2 injection, the microscopic visualization technology was employed in this study to conduct displacement experiments of CO_2/brine at the pore scale. Four micromodels with different sizes and structures, five injection rates of CO_2 and six salinities of brine were used to study the effects of micromodel's structure and displacement pattern on two-phase flow. Several parameters including the differential pressure, contact angle, permeability, velocity field and force field were obtained by experimental measurement, image post-processing and theoretical analysis, and then these parameters' variation was investigated. Phenomena such as thin film, corner flow and Haines jump were also found during the displacement. Although brine could be completely displaced by CO_2 in the capillary duct, the backflow of wetting phase would occur at low injection rate. Phenomena different from the theoretical analysis also occurred in pore doublet models: some brine was residual in the homogeneous pore doublet model at low injection rate, while the heterogeneous pore doublet model was fully occupied by CO_2 at high injection rate. These phenomena are very useful for two-phase flow, and multiple factors need to be comprehensively considered to determine the operating conditions of CO_2 storage into the brine aquifer.

1 Introduction

Fluid flow in porous media has many applications (Berejnov et al., 2008), such as oil and gas resource recovery, groundwater contamination, CO_2 geological storage (CGS) (Patmonoaji et al., 2020). As an important technology of CGS, carbon storage in the brine aquifer can achieve massive CO_2 storage and thus effectively control the global warming. The two-phase flow of CO_2/brine in the formation is a key factor for the storage capacity and security of the brine aquifer (Morais et al., 2016).

At present, a large number of experimental and simulation studies on CO_2/brine two-phase flow have been conducted. Pore structure is one of the main factors affecting flow behavior in porous media (Gaol et al., 2020). CO_2 displacement of brine in real cores is carried out by the conventional High-Temperature-High-Pressure (HTHP) experimental system to study the effects of temperature, pressure, injection flow rate and salinity of brine on the permeability and displacement efficiency (Bai et al., 2020; Chang et al., 2014; Chen et al., 2016). However, the understanding of the transport mechanism is limited by the difficulty of monitoring fluid flow in opaque media (Wu et al., 2012). With the development of technology, this problem is overcome by non-invasive image techniques such as optical imaging, gamma imaging, synchrotron X-ray microtomography and magnetic resonance imaging, which allow the visualization study of two-phase flow in real porous media at the core or pore scale. But there are still some problems with these techniques like expensive equipment, complex operation and limited temporal resolution, so that some subtle changes are easily overlooked (Werth et al., 2010).

The visualization technique of combining a microscope with a camera can simultaneously achieve high-resolution temporal and spatial measurement by adjusting the frames per second (fps) of camera and the magnification of microscope, and has been increasingly applied to the study of CO_2/brine flows in recent years. Chang et al. from Lawrence Berkeley National Laboratory have comprehensively and systematically studied the CO2/brine

displacement and imbibition under formation conditions using many micromodels with different structures, including homogeneous structure, real core structure and even 2.5-D structure, to identify the non-equilibrium dissolution, diffusion, two-phase distribution, storage capacity, and flow mechanism (Chang et al., 2017; Chang et al., 2019; Chang et al., 2020; Chang et al., 2016). On the other hand, Jafari et al. from Louisiana State University mainly focused on the micro-scale contact angles using the inhomogeneous micromodel at room temperature and high pressure during the process of CO_2 displacing brine (Jafari and Jung, 2017; 2019). Kazemifar et al. from the University of Illinois at Urbana-Champaign used the micro-PIV technique to describe the velocity field of CO_2/brine in the homogeneous micromodel under high temperature and pressure (Kazemifar et al., 2015; 2016). Nevertheless, some phenomena on the macroscopic scale have not been fully explained. Some special phenomena have been found on the microscopic scale, which need to be supplemented by more experiments and simulations. So, this study aims to conduct the CO_2 displacement of brine in four micromodels to provide the microscopic theoretical basis for flow phenomena based on the fields of velocity and force.

As early as the 1980s, visualization techniques have been used to study two-phase flow in simple micromodels. Chatzis et al. investigated the flow mechanism when displacement and imbibition of water/oil occurred in the pore doublet model in 1983 (Chatzis and Dullien, 1983). Since then, Lenormand et al. have performed lots of displacement and imbibition experiments in the capillary duct and network of capillary ducts, mainly of air/oil, and proposed the classical flow pattern on the pore scale that laid the foundation for two-phase flow (R. Lenormand and Zarcone, 1985; R Lenormand et al., 1983; Roland Lenormand et al., 1987). Subsequently, Dong et al. observed the imbibition of five different fluid pairs in a capillary duct with the rectangular cross-section and investigated the effect of channel size and fluid viscosity on the percolation rate (M. Dong, 1995). In 2009, Zhu et al. measured the contact angle and velocity field of water/air in two different capillary ducts with circular and rectangular cross-sections, respectively, combined with the theoretical analysis (Zhu and Petkovic-Duran, 2009). These studies were only using the camera with fps less than 1. So, the temporal and spatial resolution of the two-phase flow was limited. To the best of our knowledge, there is only one research where the visualization technique with a microscope combined with a camera was used to study the CO_2 displacement of brine in the capillary duct. It is Sell et al. who investigated the effects of salinity and pressure on convection and diffusion when CO_2 was injected into the curved capillary duct to displace the brine in 2013 (Sell et al., 2013). Therefore, more experiments on displacement of CO_2/brine in capillary duct or pore doublet model are needed to provide more adequate and complete mechanisms and phenomena for simulation calculations and engineering applications in the formation.

The main objective of this study is to complement the existing CO_2/brine flow mechanisms and phenomena by improving the temporal and spatial resolution using fluorescence inverted microscopy combined with high-speed camera. Two capillary ducts with different widths and two pore doublet models with different structures were used to visualize the process of CO_2 displacing brine under different capillary numbers Ca and viscous ratios M. Contact angle θ, residual brine saturation S_w and velocity field were obtained by image measurement. At the same time, CO_2 relative permeability K_{rg} and force field were obtained by experimental data combined with theoretical analysis. Finally, two-phase flow and some special phenomena in the capillary duct and the pore doublet model were described in detail, and relevant mechanisms were proposed using the obtained multiple parameters.

2 Materials and Methods

The size and connectivity of the pores and throats in the formation determine the migration pathways and sequestration capacity of CO_2 in the brine aquifer. So, two capillary ducts with different widths and two pore doublet models with different sizes were designed in this study to simplify the structure of formation and then reveal the CO_2/brine flow characteristics at the microscopic scale.

2.1 Experimental materials and conditions

Four design diagrams of micromodels are shown in Fig. 1. Two pieces of glass, 45 mm in length and 16 mm in width, were bonded together to form the micromodel that were made by Wenhao Co., Ltd. using the laser etching. Through the contact angle measurement, all micromodels in this study were hydrophilic. To mitigate the entrance/exit effect, two buffer zones consisting of cylinders were added near the entrance and exit of the micromodel, and then capillary conducts with 0.8 mm wide, 1.8 mm long were connected to the target area. The studied area had a length l of 1.1 mm. Two capillary ducts, with widths w of 0.05 mm and 0.1 mm, respectively, had a high aspect ratio, which was closer to the structure of real core. Both capillary ducts had the same w of 0.05 mm in the homogeneous pore doublet model, while the w of upper duct was 0.05 mm and the lower one was 0.07 mm in the heterogeneous pore doublet model. The etching depth d of all micromodels in this study was 0.02 mm. The pore volumes (PV) of four micromodels are shown in Table 1. All experiments were carried out at ambient temperature and pressure (25℃, 0.1 MPa) in this study.

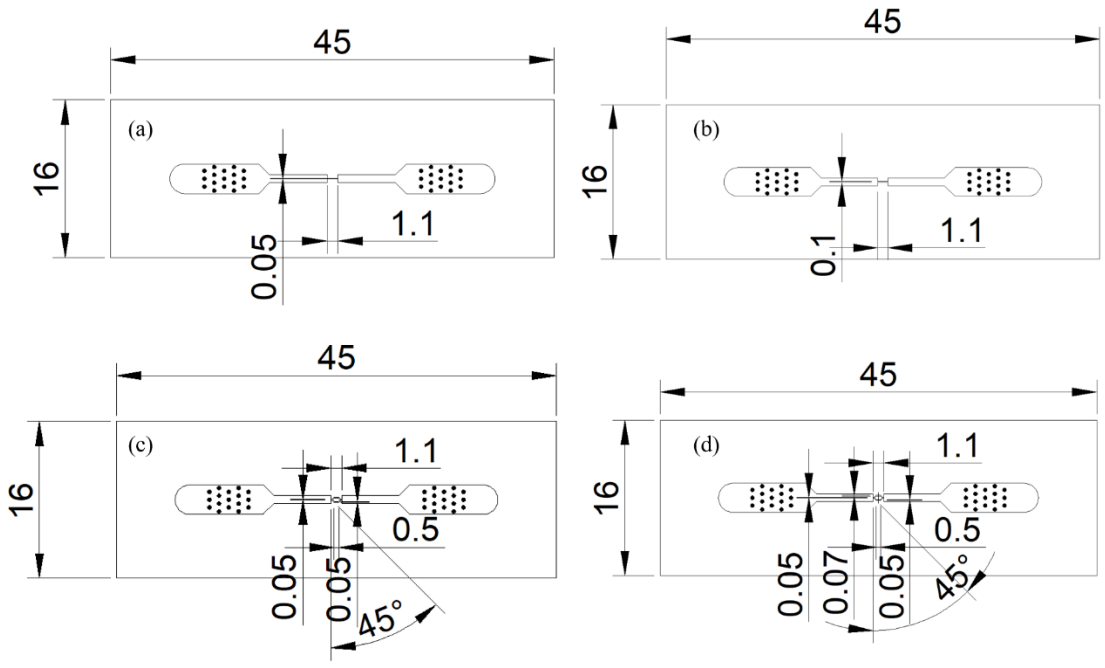

Figure 1. Design diagrams of four micromodels in mm, (a) the capillary duct with the *w* of 0.05 mm, (b) the capillary duct with the *w* of 0.1 mm, (c) the homogeneous pore doublet model, (d) the heterogeneous pore doublet model.

The effects of injection flow rate and duct size on displacement were first investigated, with CO_2 volumetric flow rate Q ranging from 0.002-0.1 ml/min, which was converted into the bulk velocity v by

$$v = Q/A \quad (1)$$

Where A is the cross-sectional area of capillary duct. Then, Ca under different conditions could be calculated by

$$Ca = \frac{\mu_2 v}{\gamma \cos\theta} \quad (2)$$

where θ was obtained by averaging advancing contact angles for each experiment, which were affected by several factors such as injection flow rate, micromodel structure and brine salinity. And the measured average advancing contact angles are shown in Tables 1 and 2. The viscosities μ_1, μ_2 of pure water and CO_2 at ambient temperature and pressure were obtained as 0.8898 and 0.0149 mPa·s, respectively, based on the NIST database. Thus, M was obtained through

$$M = \mu_2/\mu_1 \quad (3)$$

log$M$=-1.775 in this study. The interfacial tension γ between CO_2 and pure water was obtained using the empirical equation proposed by Li et al.,(Li et al., 2013) and γ=73.628 mN/m. The calculated logCa are shown in Table 1. Currently, Lenormand-Zhang phase diagram(Roland Lenormand et al., 1987; Zhang et al., 2011) is often used to determine the pattern of displacement or imbibition on the pore scale, and our distributions of log$M$-logCa in this phase diagram are shown in Fig. 2. The viscous force of wetting phase dominated in almost all displacements, when the displacement pattern was viscous fingering. At lower injection rates of 0.002 and 0.005 ml/min, the displacement pattern became crossover where both capillary and viscous forces dominated.

Table 1. Measured or calculated the bulk injection velocity v, capillary number logCa, contact angle θ, absolute permeability K and pore volume PV when CO_2 displaced pure water in different micromodels with different volumetric injection flow rates Q.

Q (ml/min)	0.05 mm wide capillary duct			0.1 mm wide capillary duct			Homogeneous pore doublet model			Heterogeneous pore doublet model		
	v (m/s)	θ (°)	logCa	v (m/s)	θ (°)	logCa	v (m/s)	θ (°)	logCa	v (m/s)	θ (°)	logCa
0.002	-	-	-	0.017	9.51	-5.465	-	-	-	0.033	16.08	-5.153
0.005	-	-	-	0.042	14.35	-5.059	-	-	-	0.083	18.80	-4.748
0.01	0.167	10.43	-4.464	0.083	23.05	-4.736	0.167	12.63	-4.460	0.167	19.81	-4.445
0.05	0.833	9.28	-3.766	0.417	28.41	-4.017	0.833	14.11	-3.759	0.833	20.39	-3.744
0.1	1.667	11.47	-3.462	0.833	14.67	-3.758	1.667	16.47	-3.453	1.667	24.11	-3.431
K (D)		3.358			15.373			11.635			11.897	
PV (μL)		0.0011			0.0022			0.002736			0.002674	

The actual brine aquifer has a certain degree of mineralization, so the effect of brine salinity on two phase flow was also studied with the salinity range of 0-2.5 mol/l in the 0.1 mm wide capillary duct at the injection rate of 0.05 ml/min. The brine viscosity, interfacial tension with CO_2 and contact angle were subsequently affected by salinity and these parameters and the corresponding log*Ca* and log*M* are shown in Table 2. The μ_1 of brine was calculated by the model proposed by Mao et al.,(Mao and Duan, 2009) and the γ and θ were calculated and measured using the same method as mentioned above. Due to the fabrication process, the contact angles at different locations of the micromodel were different due to the surface roughness even though two bonded pieces of glass were of the same material. In addition, the salinity variations would further aggravate the fluctuations of contact angles, so the θ of CO_2/brine/glass showed greater non-homogeneity at different salinities. As determined by Lenormand-Zhang phase diagram (Roland Lenormand et al., 1987; Zhang et al., 2011), the displacement pattern was viscous fingering when the brine with different salinities was displaced by CO_2 at the rate of 0.05 ml/min in the duct with the width of 0.1 mm.

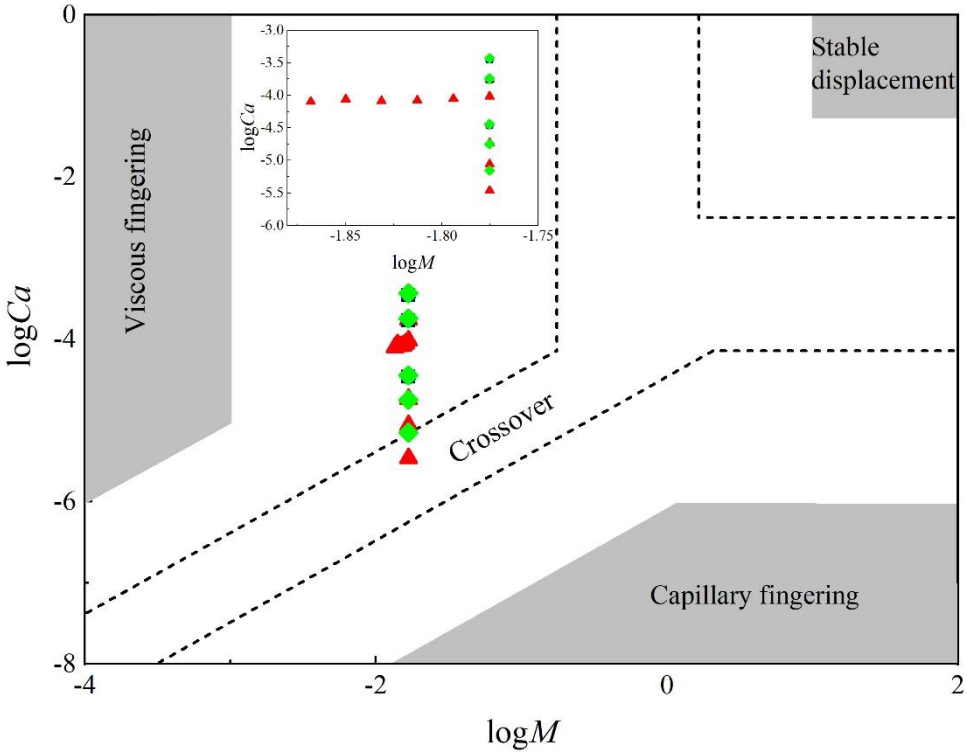

Figure 2. Distributions of log*M* and log*Ca* under different injections and salinities in the phase diagram for four micromodels: black ■, the 0.05 mm wide capillary duct, red ▲, the 0.1 mm wide capillary duct, blue ●, the homogeneous pore doublet model, green ◆, the heterogeneous pore doublet model.

Table 2. The viscosity of brine μ_1, interfacial tension between CO_2 and brine γ, contact angle θ, capillary number log*Ca* and viscosity ration log*M* when CO_2 displaced brine with different salinities in the 0.1 mm wide capillary duct at the injection flow rate of 0.05 ml/min.

Salinity (mol/l)	0	0.5	1.0	1.5	2.0	2.5
μ_1 (mPa·s)	0.8898	0.9289	0.9699	1. 0125	1.0566	1.1018
γ (mN/m)	73.628	74.860	76.047	77.190	78.292	79.356
θ (°)	28.41	19.46	11.99	10.73	-[a]	9.40
Log*Ca*	-4.017	-4.055	-4.078	-4.086	-4.062	-4.100
log*M*	-1.775	-1.794	-1.813	-1.831	-1.850	-1.868

[a] Due to the phenomenon of more intense Haines jump, the contact angle could not be measured when 2.0 mol/l brine was displaced. But θ=9.67° was used to calculate the Log*Ca* at this salinity, which was obtained using an exponential decay model (4) mentioned below.

2.2 Experimental system and procedures

The experimental system has been described in detail in the previous publication (Song et al., 2020), and the physical diagram is shown in Fig. 3. Two piston containers were connected to the same syringe pump (Teledyne ISCO 500D) to control the injection of different fluids in the constant flow model. Then they were piped to the inlet of the micromodel and the outlet was connected to atmosphere. A differential pressure gauge (Rosemount 3051) measuring from 0 to 62.2 KPa was connected between the inlet and outlet. The micromodel was placed horizontally on a fluorescent inverted microscope (Nikon, ECLIPSE Ti-2U) equipped with a 20× lens. A camera (SP-12000M-CXP4) was connected to the microscope to capture the entire flow process via a data acquisition card (KY-FGK-400).

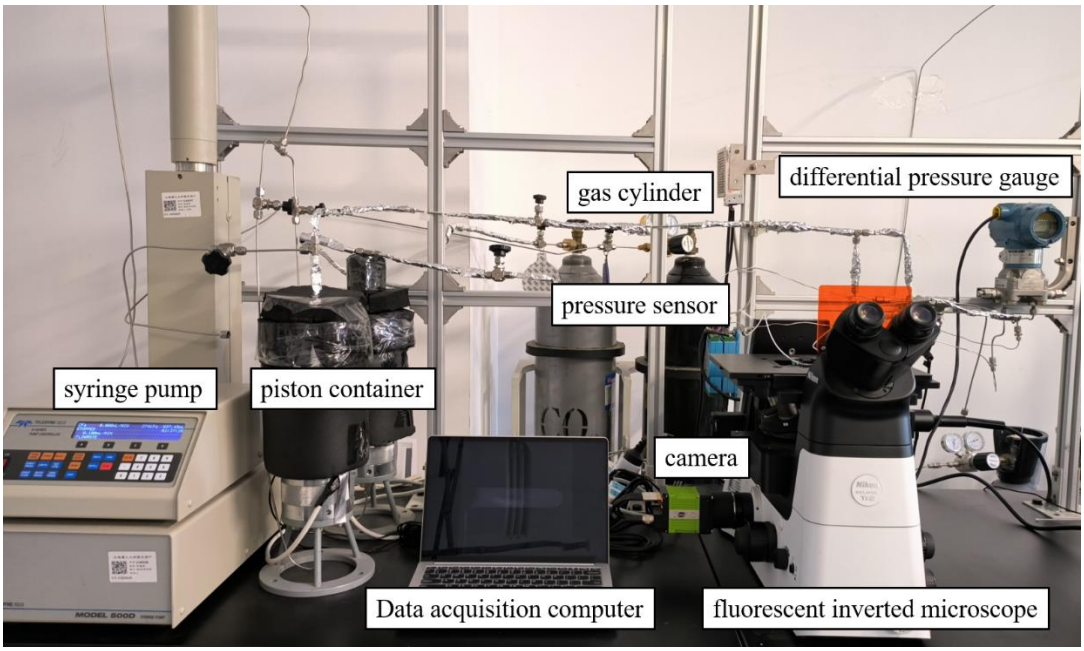

Figure 3. Physical diagram of the experimental system.

The entire system needed to be cleaned before all experiments began. Deionized water (DI), isopropanol, DI and N_2 were used for cleaning in turn, with each fluid injected at a flow rate of 0.05 ml/min for 2 h to ensure the system was cleaned thoroughly. After the cleaning, the displacement experiment started. First, the required brine was prepared. Regardless of the salinity, fluorescent dye (rhodamine B) of 0.2 g/l was added in the brine to distinguish the aqueous phase from CO_2 and micromodel. Then the dyed brine started to be injected until the micromodel was fully saturated. To measure the absolute permeability *K* of each micromodel, different injection flow rates, varying from 0.05-0.1 ml/min, were used to achieve the complete saturation of brine in different experiments. After obtaining the stable differential pressure, the absolute permeability could be calculated by Darcy's law, as listed in Table 1. Next, the injection rate was adjusted to the set value, and CO_2 began to be injected to the micromodel. When CO_2 entered the field of view (FOV), the camera started to capture pictures with fps of 50. Since the FOV was limited because of the 20× lens, the study was mainly focused on the two-phase flow near the entrance of the capillary duct or pore doublet model. When the displacement was out of the FOV, position of micromodel was manually adjusted to better track the two-phase interface. The displacement was considered to be completed when the differential pressure between the inlet and outlet remained basically stable and no further changes occurred in the FOV.

2.3 Image processing

The captured images were post-processed mainly using ImageJ and Adobe Photoshop CC 2019. Images at different locations were montaged together into the whole structure through the relationship between length and pixel using the Photoshop, thus the distribution of different phases could be obtained in the overall micromodel. ImageJ was mainly used to adjust the brightness and contrast of the image, so as to better distinguish two phases. Then the noise was removed, and the saturation of each phase was calculated by adjusting the threshold value. The specific image processing is shown in Fig. 4. The resolution of images captured in this study was 214.592 nm/pixel. Then the contact angle, velocity field and force field could be obtained through the processed image. In this study, the contact angle was measured at the interface curvature using the ellipse fitting, as shown in Fig.4(d). Due to the large capture frequency of the camera, the velocity field in the capillary duct could be obtained by the position of the interface at different times, as shown in Fig. 4(e). Due to the limitation of FOV and manual manipulation, some of the two-phase interface locations in the second half of the capillary duct were not captured. Finally, the local capillary force, viscosity resistance and total pressure drop between the entrance and exit of the duct were calculated from the two-phase interface location and the contact angle at that location.

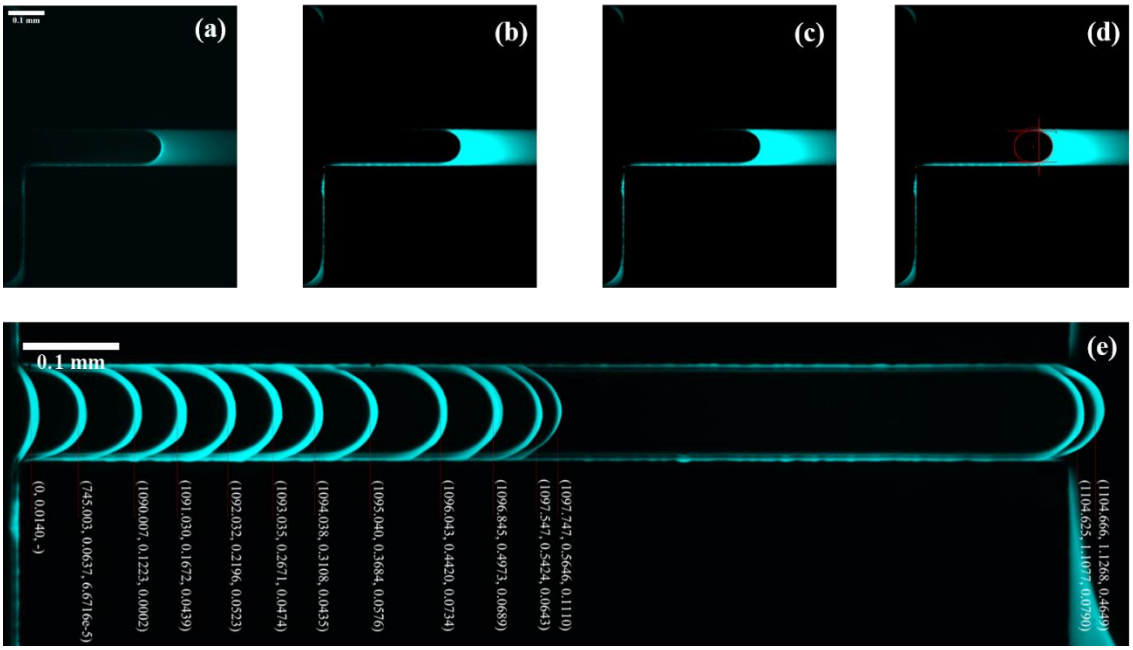

Figure 4. The specific image processing, (a) raw image, (b) image with the brightness and contrast adjusted, (c) denoised image, (d) schematic diagram of contact angle measurement, (e) montaged image, where the numbers in the parenthesis indicate (absolute time (s), distance from the two-phase interface to the entrance of the duct (mm), local velocity (m/s)). CO_2 is injected from left to right at the rate of 0.002 ml/min and cyan represents the brine.

3 Experimental Results

In this study, a total of 21 sets of displacement experiments of CO_2/brine were conducted. Through the experimental measurement and image post-processing, the differential pressure, wettability, CO_2 relative permeability, velocity field and force field were obtained to provide quantitative analysis for two-phase interface and displacement characteristics at the pore scale.

3.1 Differential pressure

The differential pressure at the inlet and outlet of the micromodel was recorded by differential pressure gauge during the entire displacement process, as shown in Fig. 5. The differential pressure was consistent with the results of previous study (Jin et al., 2020), and the whole process could be roughly divided into three stages: accumulation stage, breakthrough stage and stabilization stage, as shown in Fig. 5 when the injection rate was 0.1 ml/min.

In the pressure accumulation stage, as the injected PV increased, CO_2 kept accumulating at the inlet of the micromodel and was compressed. CO_2 could not displace the brine in the duct until the accumulated pressure reached the critical breakthrough pressure p_c. Whether it was a capillary duct or a pore doublet model, the accumulation stage was clearly divided into two processes. Pressure built up rapidly when CO_2 was injected from the inlet of the micromodel and reached the entrance of the duct through the buffer region. Once CO_2 reached the entrance, the build-up rate of pressure decreased and CO_2 started to be compressed, gradually forming a curved interface with the aqueous phase. These two different processes of the accumulation stage

were approximated as two lines with different slopes, as shown in Fig. 5. When the accumulated pressure reached the p_c, CO_2 started to enter the capillary duct or the pore doublet model to displace the brine, and the two-phase interface moved along the flow direction or in the reverse direction. As the interface moved forward, the differential pressure decreased until the breakthrough. Compared to the accumulation stage, the breakthrough stage proceeded very fast. Therefore, the breakthrough time t_b was defined when differential pressure increased from 0 to p_c. For better comparison, the injected PV was used in this study to represent the displacement time. After the breakthrough, stability was basically achieved for the differential pressure, accompanied with some fluctuations owing to the continuous injection of CO_2.

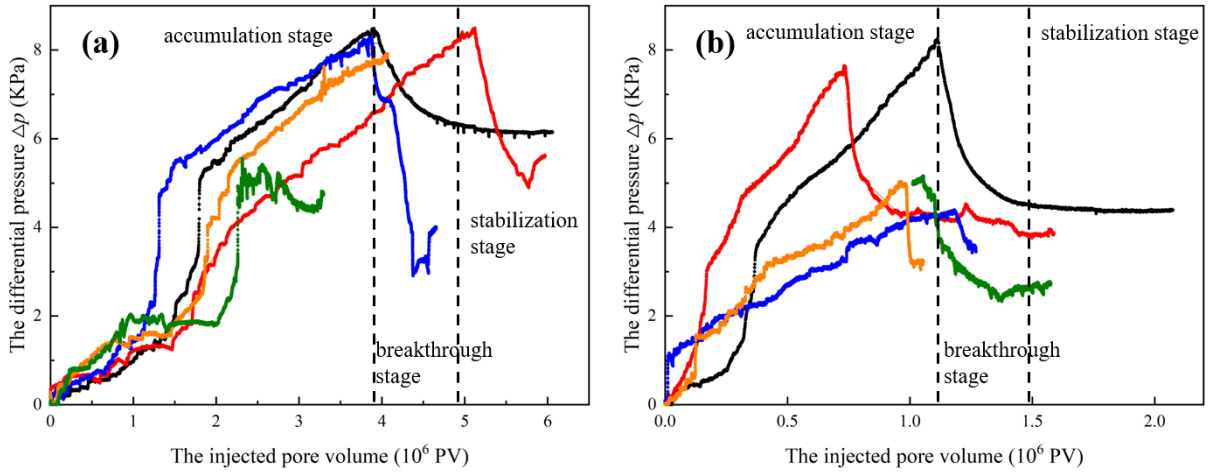

Figure 5. The development of the differential pressure $\triangle p$ with the injected pore volume at different injection rates marked by lines of different colors: black line-0.1 ml/min, red line-0.05 ml/min, blue line-0.01 ml/min, orange line-0.005 ml/min, green line-0.002 ml/min, in different micromodels: (a) the capillary duct with the width of 0.1 mm, (b) the heterogeneous pore doublet model. Two black dotted lines divide the process into three stages in two micromodels at the rate of 0.1 ml/min: accumulation stage, breakthrough stage and stabilization stage.

In general, breakthrough time t_b, critical pressure p_c and stabilization pressure p_s are three important characteristic parameters during the displacement. It can be seen from Fig. 5 that these three parameters were related to the structure of micromodel and injection flow rate. The relationship between these three parameters and capillary numbers in four micromodels is summarized in Fig. 6. For the capillary duct, the PV injected to reach the p_c basically increased with log*Ca*, indicating that the increased injection rate does facilitate more CO_2 injection during the pressure accumulation stage. In contrast, the PV injected to reach the p_c in the pore doublet model was not much affected by log*Ca*, with the average value $t_b=1.36\times10^6$ PV in the homogeneous pore doublet model and $t_b=0.99\times10^6$ PV in the heterogeneous pore doublet model. But one thing was consistent with the result in the capillary duct, that was, the increase in width decreased the displacement time, i.e., the larger pores and throats will accelerate the process of displacement. As for p_c and p_s, the value of p_s was smaller than p_c, but the trend with log*Ca* was basically the same. Both pressures increased with the injection rate, which was related to the increase of viscous force in the capillary duct or pore doublet model. The difference between p_c

and p_s remained essentially constant in the 0.05 mm wide capillary duct and homogeneous pore doublet model. The average value of this difference in the 0.05 mm wide capillary duct was 1.60 KPa. While in the homogeneous pore doublet model, due to an additional 0.05 mm wide capillary duct, this difference doubled to an average value of 3.99 KPa. In the other two micromodels, this difference was more complex, partly due to the structure, and partly due to a shift of the displacement pattern.

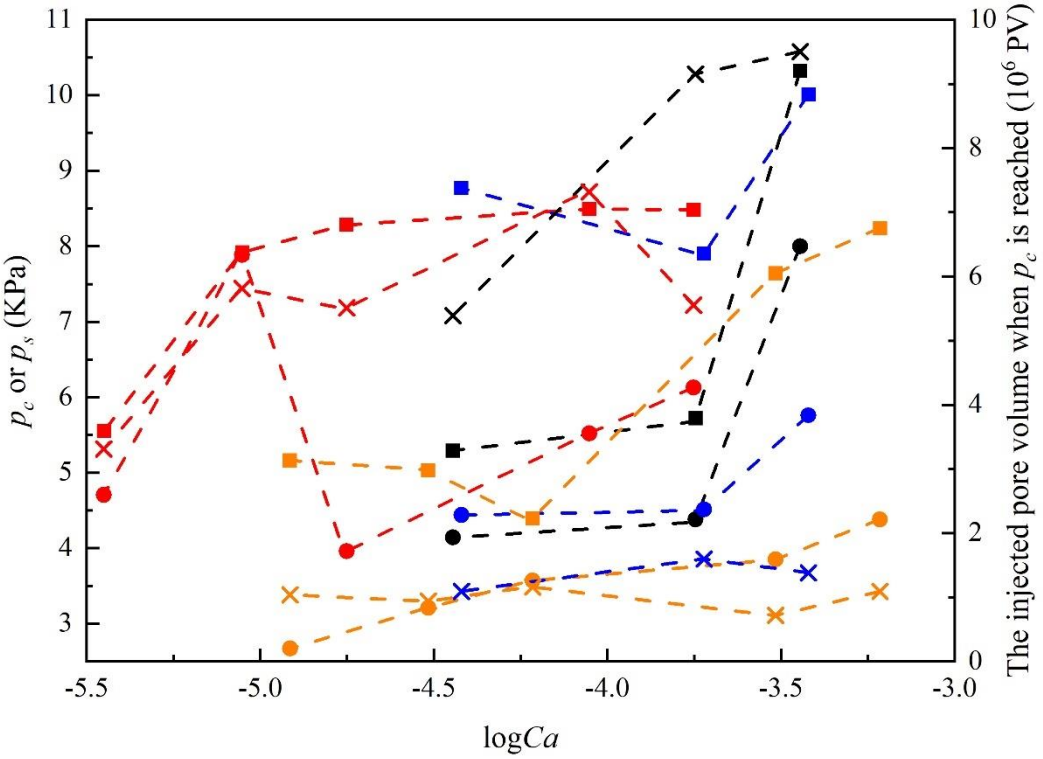

Figure 6. Variation of the injected pore volume when p_c is reached (×), maximum differential pressure p_c (■) and the stabilization differential pressure p_s (●) with log*Ca* in four micromodels marked by lines of different colors: black-0.05 mm wide capillary duct, red-0.1 mm wide capillary duct, blue-homogeneous pore doublet model, orange-heterogeneous pore doublet model.

The salinity of brine also had an important effect on the differential pressure. From Fig. 7, it was clear that the effect of salinity on displacement was more complex caused by the wettability. Besides direct change in the viscous force, the capillary force was also affected when CO_2 displaced brine with different salinities in this study, and the contact angle was an important parameter to calculate the capillary force. The roughness of micromodel coupled with the salinities of brine led to more complex θ, which resulted in larger fluctuation of the capillary force to further affect the force field. In the salinity range of 0-2.5 mol/l, the relationship between differential pressure and salinity was not significant. Compared to pure water, the presence of salinity led to faster breakthrough and larger values of p_c and p_s. It can be seen that the variation of p_c and p_s with salinity was complicated, but the trends were similar. At the salinity of 2.0

mol/l, the largest p_c, the largest p_s and the fastest breakthrough were achieved, which caused the more intense Haines jump that would be described in detail later.

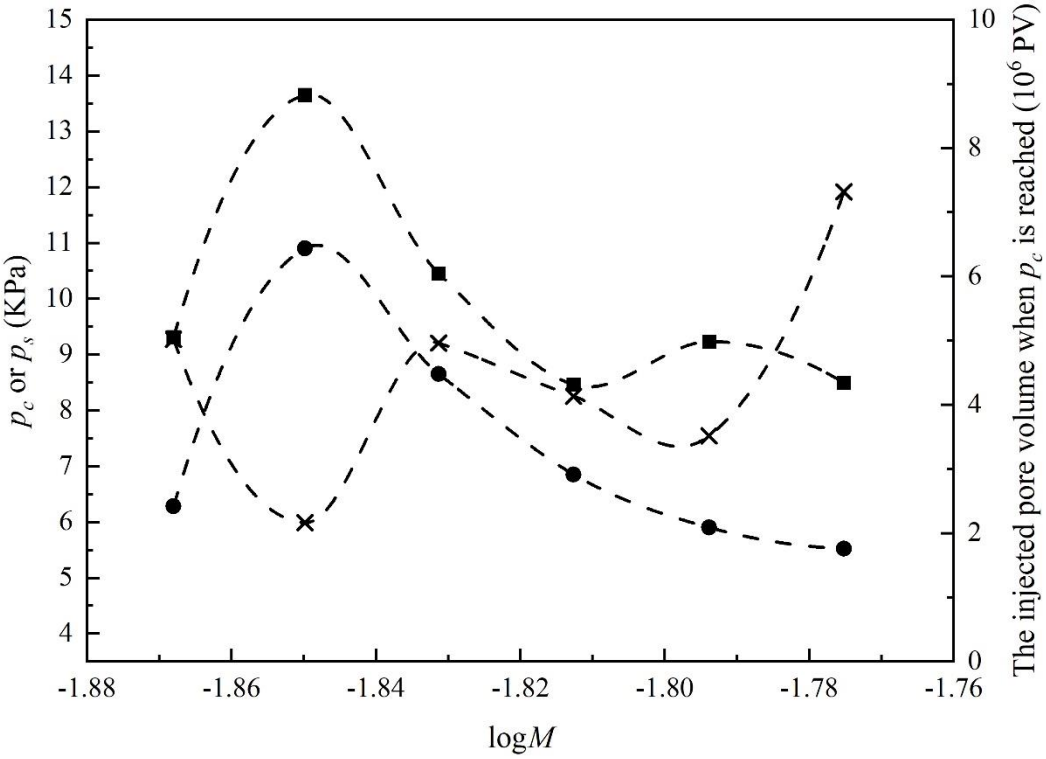

Figure 7. Variation of the injected pore volume when p_c is reached (×), maximum differential pressure p_c (■) and the stabilization differential pressure p_s (●) with log$M$ in the 0.1 mm wide capillary duct with CO_2 injection flow rate of 0.05 ml/min.

In conclusion, injection flow rate, structure of micromodel and salinity of brine all affect the differential pressure during CO_2 sequestration into the brine aquifer, which is comprehensive and complex. Thus, the optimal CO_2 injection flow rate needs to be determined by considering the geological structure and brine mineralization.

3.2 Contact angle

Wettability not only affects the capillary number, but also has an important role in the capillary force and flow process. Static contact angle is generally used to calculate the capillary number, but it has been proved that there is a certain deviation in the static contact angle and dynamic contact angle, and even hysteresis between the advancing contact angle and receding contact angle (Jafari and Jung, 2019). Therefore, it was more accurate to calculate the *Ca* using the advancing contact angle in this study. By elliptically fitting the curved interface, advancing contact angles at different positions of the same micromodel were measured, and then the contact angle used for calculation of *Ca* was obtained by averaging advancing contact angles. Due to the fabrication, different degrees of roughness existed on the surface of the same micromodel, which resulted in different wettability at different locations, as shown in Fig. 8, the standard deviations

of the θ were relatively large. The average value of the advancing contact angle obtained in this study was less than 30° in all four micromodels, so the materials used in this study were considered as strongly hydrophilic. It can be seen from Fig. 8 that the average θ increased with the injection flow rate. The increase in the injection flow rate led to an increase of the viscous force, thus reducing the wall hysteresis effect and a smaller equivalent radius of the fitted ellipse, which resulted in a larger contact angle. As the salinity of brine increased, the advancing contact angle would be inhibited because of the raised intermolecular forces between the brine and structure. And this can be quantified by an exponential decay model, which was obtained by fitting the experimental data:

$$\theta = 8.702 + 20.624e^{\frac{0.040-x}{0.642}} \quad (4)$$

where x was the salinity of brine, and R-Square was 0.97315.

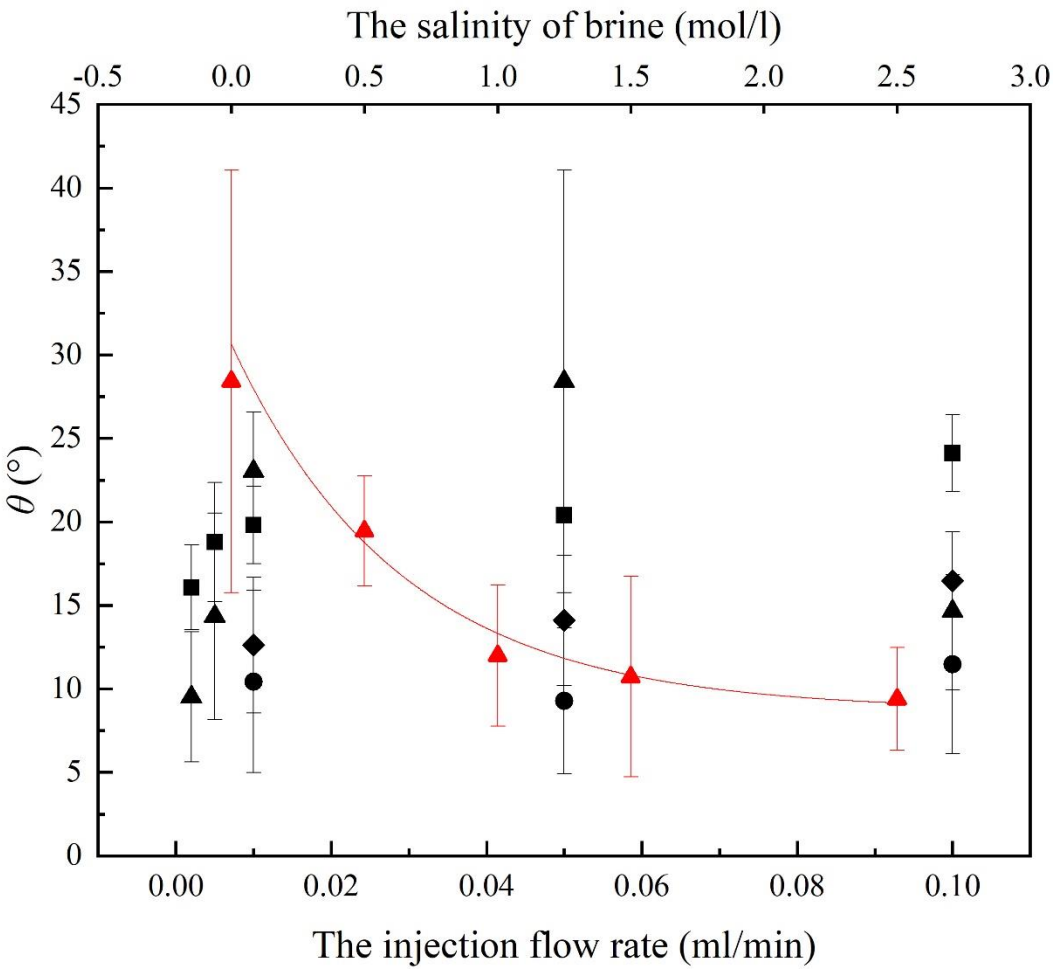

Figure 8. Variation of the average advancing contact angle θ with standard deviations with the injection flow rate and salinity of brine in four micromodels: ●, the 0.05 mm wide capillary duct, ▲, the 0.1 mm wide capillary duct (black, as injection rate and red, as salinity), ◆, the homogeneous pore doublet model, ■, the heterogeneous pore doublet pore.

358

359 3.3 CO_2 relative permeability

360 CO_2 relative permeability plays an important role in the mobility and migration pathway
361 of carbon in the formation. Based on the experimental process and measurement method of this
362 study, the CO_2 relative permeability was calculated using formulas proposed by Huang et al
363 (Huang Daming, 1984):

$$K_g = \frac{2LQP_0Z_a\mu_2}{A(P_1^2 - P_2^2)Z_0} \quad (5)$$

364

$$K_{rg} = \frac{K_g}{K} \quad (6)$$

365 Where K_g is the CO_2 effective permeability, K_{rg} is the CO_2 relative permeability, P_0 is the
366 atmospheric pressure, P_1 is the inlet pressure of the micromodel, P_2 is the outlet pressure of the
367 micromodel, Z_0 is the compression coefficient of CO_2 at P_0 and experimental temperature, and Z_a
368 is the compression coefficient of CO_2 at the average pressure of P_1 and P_2 and experimental
369 temperature. Therefore, CO_2 relative permeability after breakthrough was calculated using
370 equations (5) and (6) for four micromodels and different salinities, as shown in Figures 9 and 10.

371

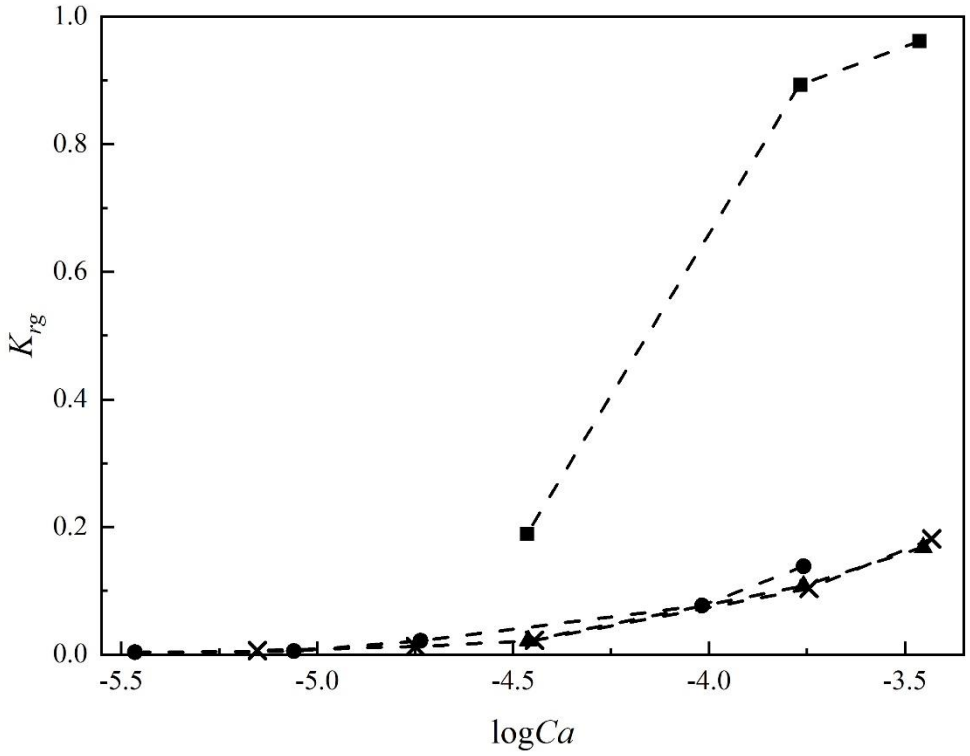

372

373 **Figure 9**. Variation of CO_2 relative permeability K_{rg} with logCa in four micromodels: ■, the
374 0.05 mm wide capillary duct, ●, the 0.1 mm wide capillary duct, ▲, the homogeneous pore
375 doublet model, ×, the heterogeneous pore doublet model.

376

Consistent with the simulation results of Juanes et al.(Juanes, 2006), CO_2 relative permeability would increase with the injection rate. In other words, as the injection rate increases, the mobility of injected CO_2 in the formation is enhanced after the displacement, and risks of fugitive flow and carbon leakage are more likely to occur. This enhancement was more obvious in the 0.05 mm wide capillary duct, which proves that this type of structure was not conducive to CO_2 sequestration. The comparison in four micromodels revealed that the CO_2 relative permeability would decrease when the width of capillary duct changed from 0.05 mm to 0.1 mm and the structure changed from capillary duct to pore doublet model. As shown in Fig. 10, with the presence of salinity, CO_2 relative permeability after the breakthrough would be smaller than that obtained when pure water was displaced. This was consistent with the result from Bachu et al.(Bachu and Bennion, 2008), who proved it through displacement and imbibition experiments with different cores. In the 0.1 mm wide capillary duct, CO_2 relative permeability decreased by 50.64% when the displaced phase changed from pure water to 2.0 mol/l brine. However, CO_2 relative permeability would increase to 0.067 with further increase in the salinity (2.5 mol//l in this study), which may be the result of salting out. As shown in Fig. 11, salting out occurred near the exit of the capillary duct after the breakthrough when 2.5 mol/l brine was displaced by CO_2. As the salt continued to be precipitated, the width near the exit became narrower. As the phenomenon mentioned above, CO_2 relative permeability was greater in the narrower capillary duct, so CO_2 relative permeability did not continue to decrease due to the salting out when the salinity exceeded 2 mol/l.

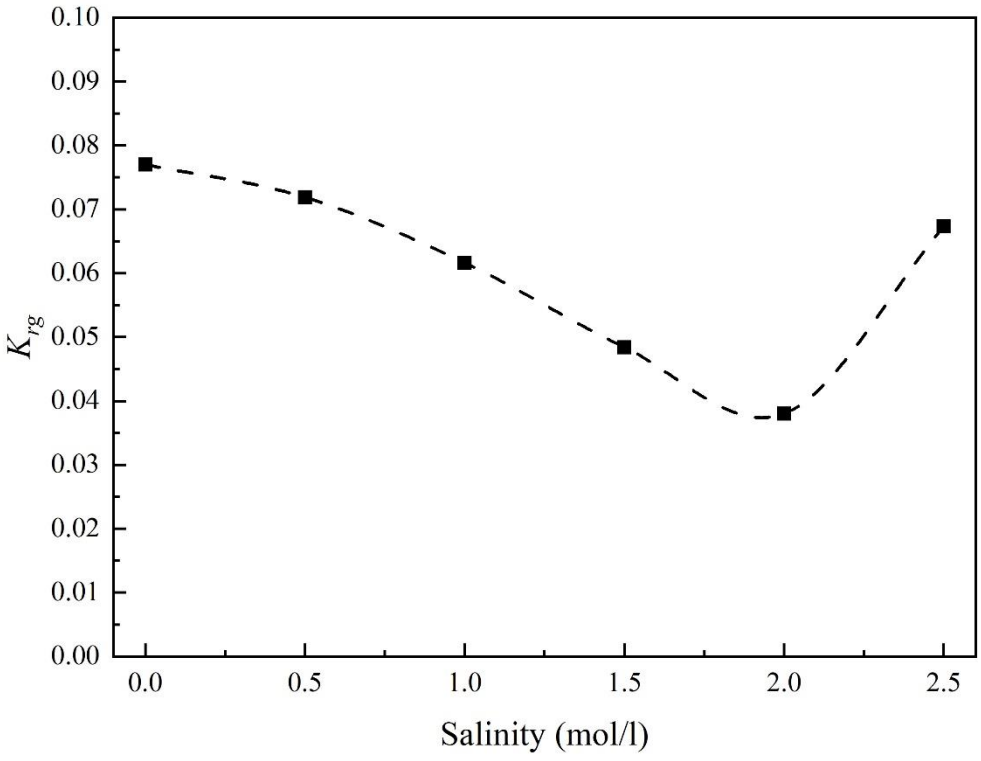

Figure 10. Variation of CO_2 relative permeability K_{rg} with salinity of the brine in the 0.1 mm wide capillary duct after the breakthrough with CO_2 injection rate of 0.05 ml/min.

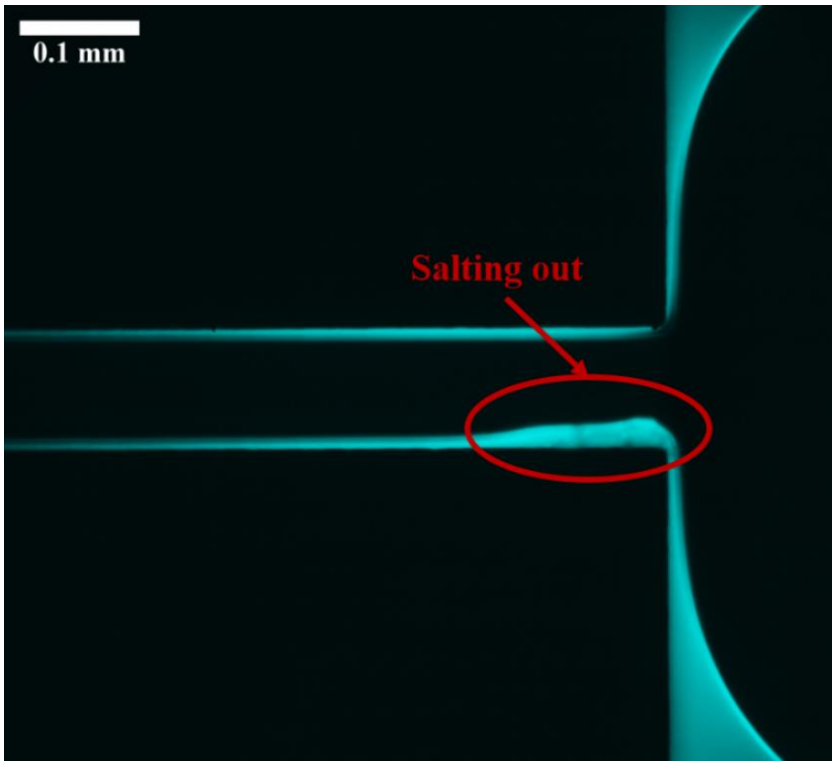

Figure 11. Salting out near the exit of the 0.1 mm wide capillary duct after the breakthrough. The injection direction is from left to right, and cyan represents the brine with the salinity of 2.5 mol/l.

3.4 Velocity field

In this study, the fps of camera was set to 50, which was sufficient to capture the displacement process. The positions of CO_2/brine interface at different moments were obtained from the montaged images, as shown in Fig. 4(e), and the local velocity u could be calculated using the interface distance $\triangle x$ in the adjacent time $\triangle t$:

$$u = \frac{\Delta x}{\Delta t} \quad (7)$$

The variation of local velocity with the interface position from the entrance of the capillary duct under different conditions is shown in Figures 12 and 13. Compared with the bulk injection flow rate Q, as shown in Table 1, the calculated local velocity was about 3 orders of magnitude smaller in the capillary duct. As can be seen from Fig. 12, the displacement pattern had an important effect on the velocity field. When the injection flow rate was large, the displacement pattern was viscous fingering, and the velocity fluctuation in the duct was quite great. When the pattern gradually changed to the crossover, the velocity distribution was more uniform along the displacement direction. Due to the entrance/exit effect, the local velocity was relatively small at the entrance and exit of the capillary duct. An abrupt change in velocity, i.e., Haines jump, would occur in the pattern of viscous fingering, and this phenomenon basically occurred in the first half of the capillary duct. In the second half, the viscous force decreased as

the reduction of the aqueous phase, thus the pressure drop was not sufficient to generate Haines jump. The local velocity u was negative at some positions in the 0.05 mm wide capillary duct, i.e., the backflow of aqueous phase occurred at that position, and the same phenomenon was observed when CO_2 displaced the brine with the salinity of 0.0, 1.0 and 1.5 mol/l in the 0.1 mm wide capillary duct, as shown in Fig. 13. This will be described in detail in the next section. The occurrence of salinity can reinforce the fluctuation of the velocity field, making Haines jump more obvious. It was also found that an abrupt increase of velocity to a certain value would be maintained for a period of time, but would decrease back to the lower velocity when the pressure drop was not sufficient to maintain the higher velocity.

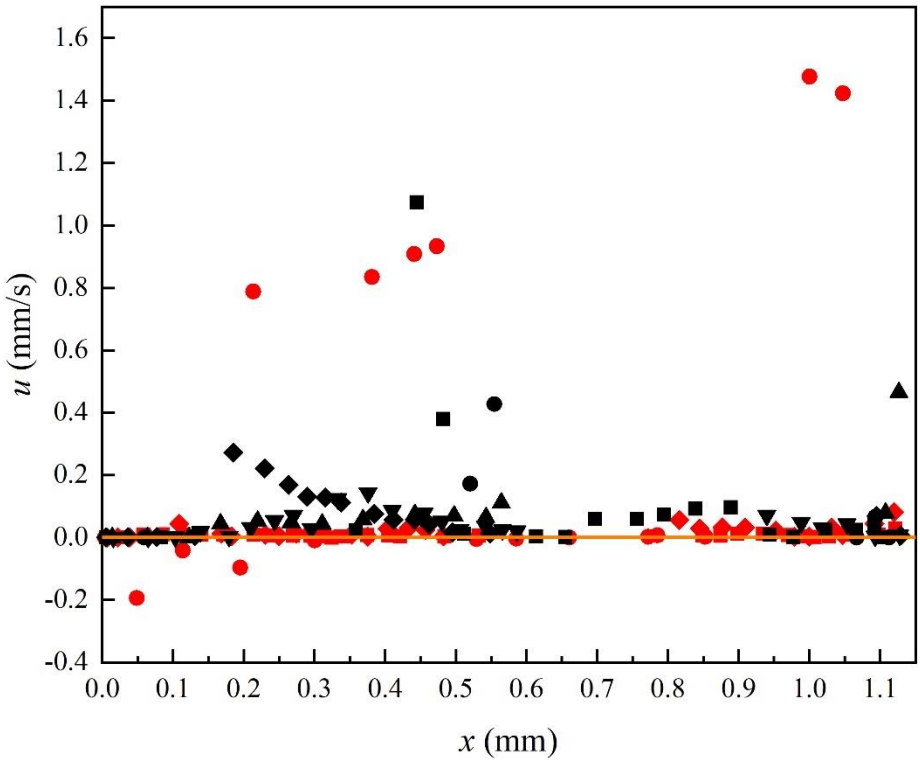

Figure 12. The local velocity u at different interface locations x from the entrance in the capillary duct with the widths of 0.05 mm (marked in red) and 0.1 mm (marked in black) at different injection flow rates: ▲, 0.002 ml/min, ▼, 0.005 ml/min, ●, 0.01 ml/min, ■, 0.05 ml/min, ◆, 0.1 ml/min. The yellow line is the base line with the velocity of 0.

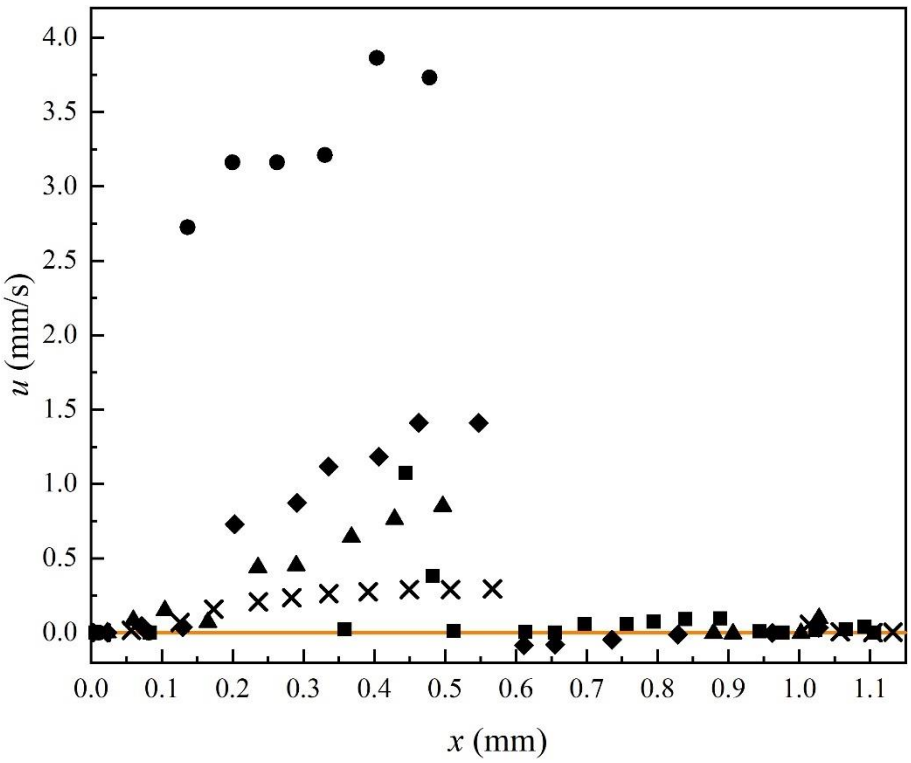

Figure 13. The local velocity u at different interface locations x from the entrance in the capillary duct with the width of 0.1 mm when CO_2 was injected at the rate of 0.05 ml/min to displace the brine with different salinities: ■, 0.0 mol/l, ●, 0.5 mol/l, ▲, 1.0 mol/l, ◆, 1.5 mol/l, ×, 2.5 mol/l. The yellow line is the base line with the velocity of 0.

3.5 Force field

The differential pressure measured by differential pressure gauge was not exactly equal to the pressure drop between the entrance and exit of the capillary duct or pore doublet model. The piping between the differential pressure gauge and micromodel, the buffer zone near the entrance and exit and the entrance/exit effect were the main reasons for this difference. Combined with the theoretical analysis, the force field in the capillary duct was calculated without considering the influence of these factors, as shown in Figures 14 and 15.

When immiscible flow occurs in the capillary duct, the overall pressure drop $\triangle P$ between the entrance and exit is composed of viscous pressure $\triangle P_v$ and capillary pressure $\triangle P_c$:

$$\triangle P = \triangle P_v + \triangle P_c \quad (8)$$

where $\triangle P_v$ is calculated by the modified Hagen-Poisson flow by Mortensen et al.,(Mortensen et al., 2005) where the effect of the shape factor α is taken into account:

$$\triangle P_v = \alpha \frac{Q\mu L}{A^2} \quad (9)$$

where μ is the effective viscosity of two fluids in the capillary duct:

$$\mu = \frac{x}{L}\mu_2 + \frac{L-x}{L}\mu_1 \quad (10)$$

where x is the distance from the entrance to two-phase interface. The shape factor α is related to the cross-section of the duct, which is rectangular in this study. The relationship between α and the dimensionless number of shape C for the rectangular cross-section was proposed by Mortensen et al.(Mortensen et al., 2005) as follows:

$$\alpha(C) = \frac{22}{7}C - \frac{65}{3} + O([C-18]^2) \quad (11)$$

$$C = \frac{p^2}{A} \quad (12)$$

where p is the perimeter of the cross-section. Then $\triangle P_v$ at different interface locations is calculated by bringing equations (10)(11)(12) into equation (9).

Due to the rectangular cross-section used in this study, the capillary pressure at different interface locations was calculated using the modified Young-Laplace equation by Juncker et al.(Juncker et al., 2002):

$$P_c = 2\sigma\cos\theta\left(\frac{1}{w} + \frac{1}{d}\right) \quad (13)$$

Combining equations (9) and (13), the total pressure drop $\triangle P$ during the displacement can be calculated using equation (8), and the fields of three pressures, local capillary force $\triangle P_c$, viscous force $\triangle P_v$ and overall pressure drop $\triangle P$, are shown in Figures 14-16. The results further confirmed that the two-phase flow was closely related to the width of duct, interface location, injection flow rate, contact angle and salinity.

In this study, the displacement patterns were viscous fingering and crossover according to the phase diagram, thus the viscous force played an important role for the two-phase flow. The $\triangle P_v$ decreased linearly as the interface moved toward the exit of the duct. Because the viscosity of CO_2 is much less than brine, the $\triangle P_v$ near the entrance was basically caused by the brine. As displacement proceed, the brine was continuously displaced, causing a decrease in the effective viscosity. After breakthrough, the viscous force in the duct was essentially from CO_2. As for the capillary force, the heterogeneity of wettability was the main reason for its fluctuation at different locations in the same duct. Comparing three pressures in two capillary ducts with different widths, it was found that the $\triangle P$, $\triangle P_v$ and $\triangle P_c$ were greater in the narrower duct. This was why larger injected PV was needed to achieve the displacement in the 0.05 mm wide capillary duct.

It was found through Figures 14 and 15 that the displacement pattern had a large effect on the pressure field. When viscous fingering occurred, the viscous force of the displaced phase would be greater than the capillary force and dominated the displacement. But this difference gradually decreased as interface moved toward the exit of the duct, and the capillary force would be greater than viscous force due to the almost absence of brine near the breakthrough. Therefore, there must exist a position where $\triangle P_v = \triangle P_c$, and then the displacement pattern transformed from viscous fingering to crossover, and as the interface continued to advance, the

capillary force dominated and then capillary fingering would occur. As the flow rate increased, the location where this pattern shift occurred was closer to the exit. At lower injection rate in this study, the crossover occurred near the entrance of the duct, where $\triangle P_v=\triangle P_c$ or $\triangle P_v<\triangle P_c$. Capillary fingering would occur as the interface moved toward the exit when the capillary force dominated. As can be seen, the viscous force decreased little at lower flow rate, so the probability of the displacement pattern shift was small. Even if it did, the position was closer to the exit of the duct.

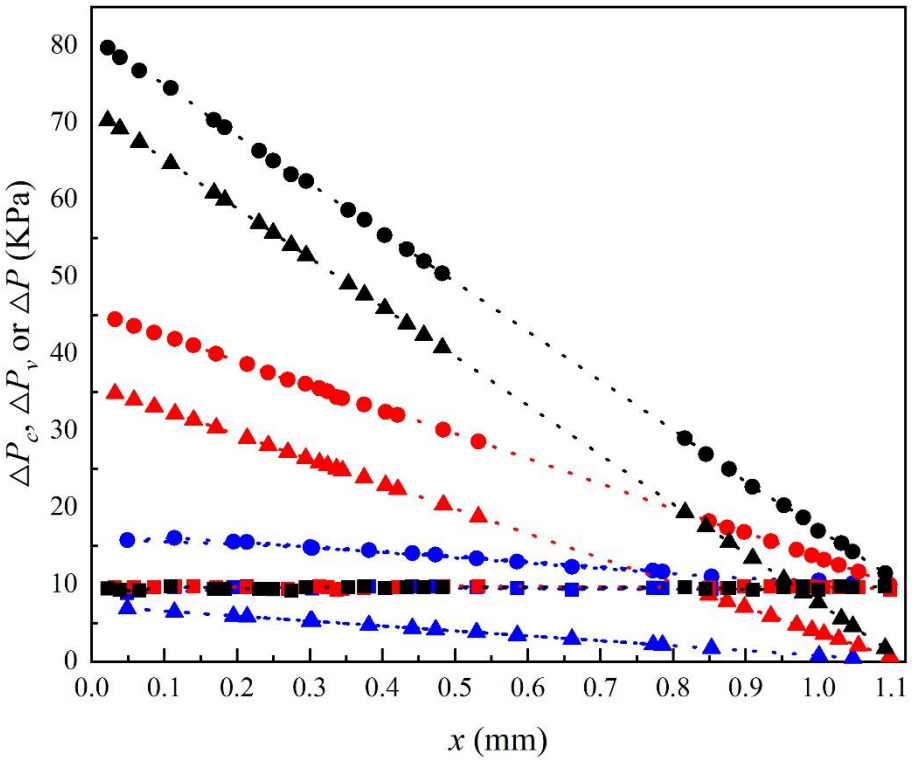

Figure 14. The local capillary force $\triangle P_c$ (■), viscous force $\triangle P_v$ (▲) and overall pressure drop $\triangle P$ (●) at different interface locations x from the entrance at different injection rates: 0.01 ml/min (marked in blue), 0.05 ml/min (marked in red) and 0.1 ml/min (marked in black) in the 0.05 mm wide capillary duct.

The effect of the salinity of brine on the force field is shown in Fig. 16. As the salinity increased, the viscous force increased when the interface was near the entrance of the duct, and thus the total pressure drop also increased. But the viscous force caused by salinity decayed as the two-phase interface moved toward the exit, causing almost same values of $\triangle P$ at different salinities near the exit of the duct. Therefore, in the capillary duct of this study, salinity affected the displacement mainly by changing the viscous force near the entrance and had little effect on the flow behavior near the exit. Comparing with Figure 7, it can be found that although the relationship between salinity and force field was obvious, the variation of measured differential pressure with salinity was more complicated. Therefore, it was concluded that the effects of pipeline, buffer zone and entrance/exit effect could not be negligible. So, the location and length

of the injection wellbore should not be underestimated when CO_2 is injected into the brine aquifer, and this is the focus of our next research.

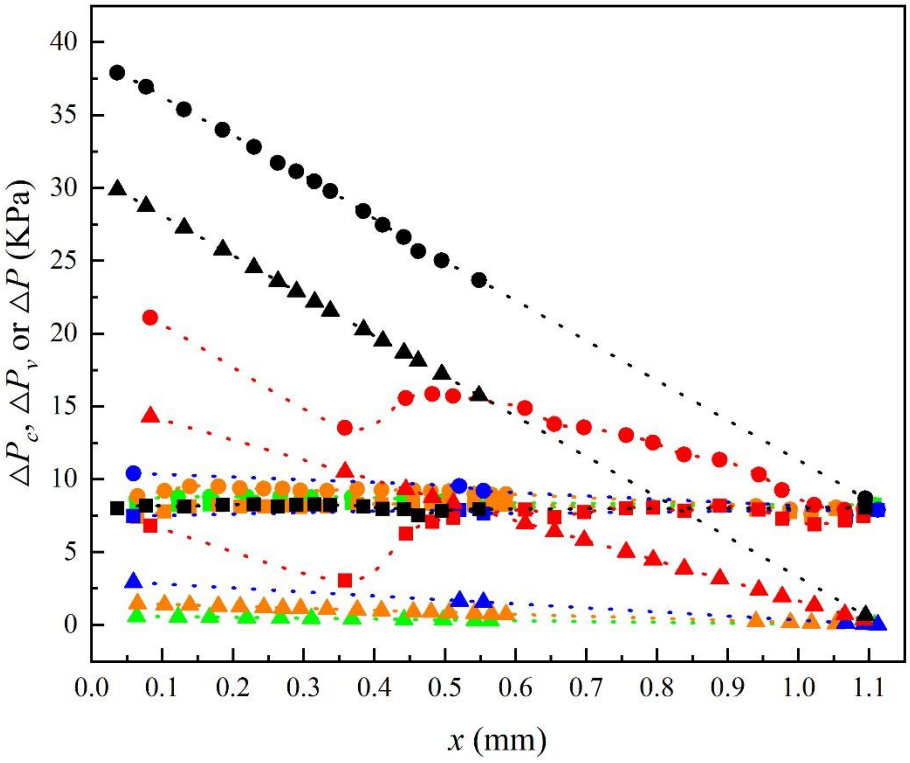

Figure 15. The local capillary force $\triangle P_c$ (■), viscous force $\triangle P_v$ (▲) and overall pressure drop $\triangle P$ (●) at different interface locations x from the entrance at different injection rates: 0.002 ml/min (marked in green), 0.005 ml/min (marked in orange), 0.01 ml/min (marked in blue), 0.05 ml/min (marked in red) and 0.1 ml/min (marked in black) in the 0.1 mm wide capillary duct.

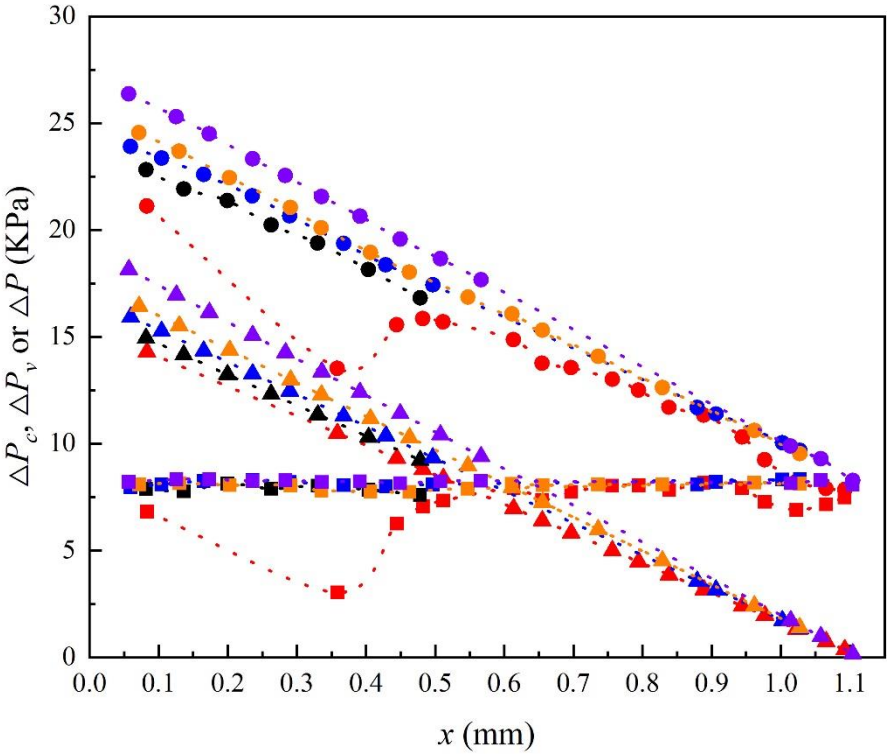

Figure 16. The local capillary force (■), viscous force (▲) and overall pressure drop (●) at different interface locations x from the entrance when CO_2 was injected at 0.05 ml/min to displace the brine with different salinities: 0.0 mol/l (marked in red), 0.5 mol/l (marked in black), 1.0 mol/l (marked in blue), 1.5 mol/l (marked in orange) and 2.5 mol/l (marked in purple) in the 0.1 mm wide capillary duct.

4 Analysis and Discussion

4.1 The flow in the capillary duct

The critical pressure to be overcome for CO_2 to enter the duct would be higher with narrower duct and larger injection rate, as described in the force field section. As a result, the injected PV and displacement time required from the start of displacement to breakthrough increased, and a higher differential pressure was maintained after the breakthrough. So, the large injection flow rate, pore and throat are not conducive for the safety of CO_2 storage into the brine aquifer. Although the lower differential pressure after breakthrough at lower injection flow rate is favorable for the safety of CO_2 storage, it takes more time to complete the displacement. In terms of economics, it is also inappropriate to use low CO_2 injection flow rates in practical engineering applications. Overall, no matter what duct width and injection flow rate were used, breakthrough would always occur in the single capillary duct, and after the breakthrough, the CO_2 saturation was basically up to 100% without considering the residual thin films of the wetting phase due to the strong hydrophilicity. However, the t_b, p_c and p_s all varied with the duct width and flow rate, and the combined effect of these parameters is critical to the application of CO_2 storage into the brine aquifer.

552

553 **Table 3.** The situations when backflow occurred and its location, time and number.

Width of the capillary duct/mm	Salinity of the brine/mol/l	CO_2 injection rate/ml/min	Location of the backflow/mm	Time of the backflow/s	Number of the backflow
0.05	0	0.01	0.7856/0.7726	43.833/1157.886	2
0.05	0	0.05	0.3450	470.007	1
0.1	0	0.01	1.0930	2665.726	1
0.1	1.0	0.05	1.0279	7.520	1
0.1	1.5	0.05	1.0276	17.084	1

554

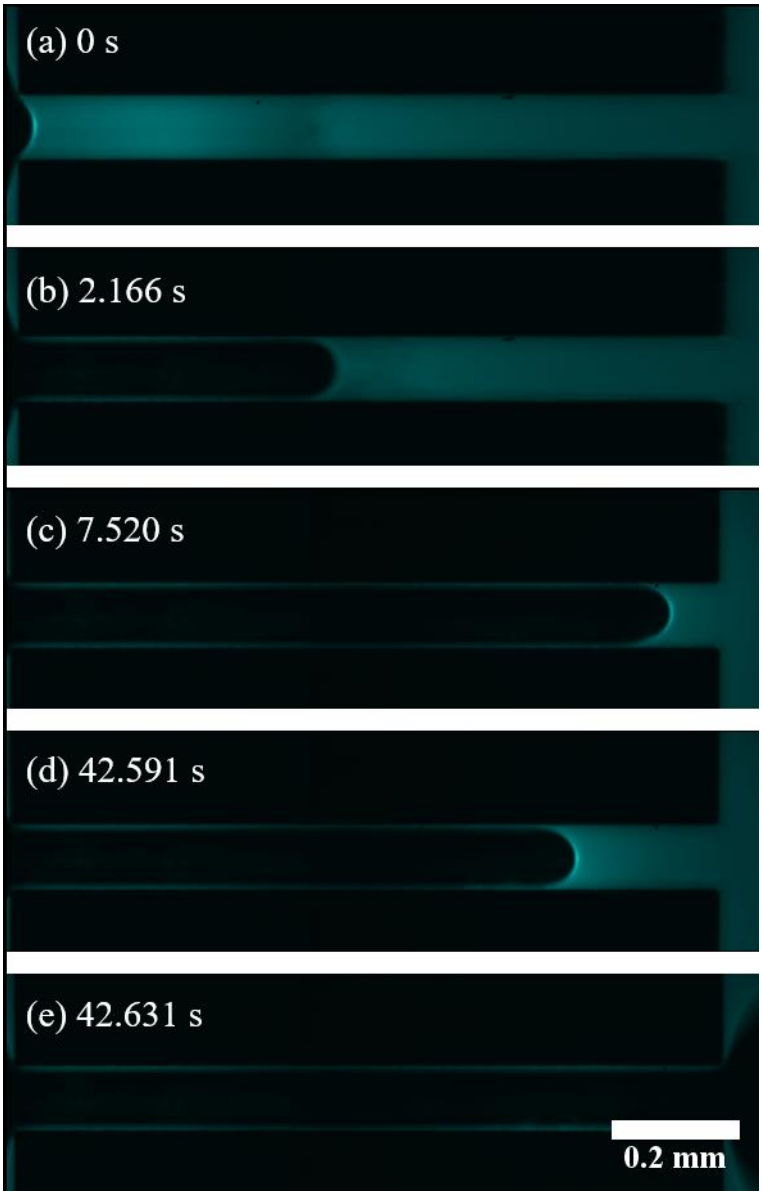

555

Figure 17. The backflow of wetting phase in the 0.1 mm wide capillary duct when 1.0 mol/l brine was displaced by CO_2 at the injection rate of 0.05 ml/min.

The velocity field showed that the local velocity at some positions was negative, and the backflow of wetting phase occurred at this point, as shown in Figure 17. The situations when backflow occurred and the corresponding location, time and number are listed in Table 3. Two backflows occurred before the final breakthrough when CO_2 was injected at the rate of 0.01 ml/min in the 0.05 wide capillary duct and the breakthrough was achieved with only one backflow in other situations. In general, there was a high probability of backflow when CO_2 displaced brine at an intermediate rate, i.e., 0.01 and 0.05 ml/min, in this study. Therefore, there was sufficient reason to believe that the displacement at these two injection rates should be attributed to crossover, rather than viscous fingering defined in the traditional phase diagram, as shown in Fig. 2. Correspondingly, when the injection rate was less than 0.01 ml/min, the displacement pattern was capillary fingering instead of crossover. It is demonstrated that *Ca* and *M* are not the only parameters to determine the displacement pattern (Bakhshian et al., 2019).

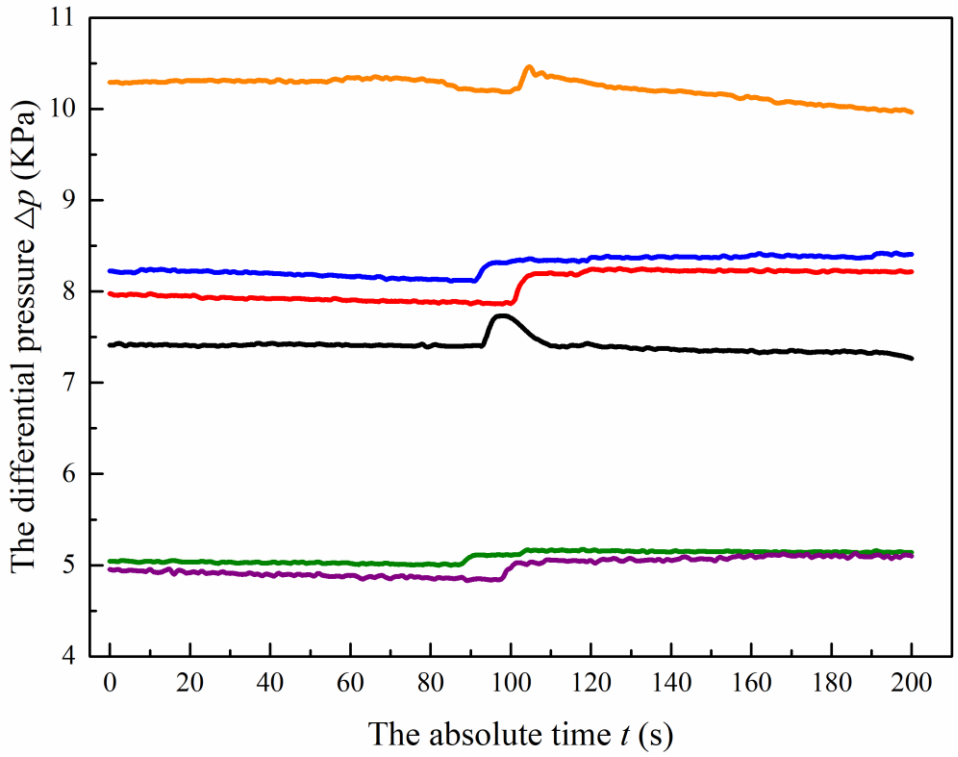

Figure 18. local differential pressure $\triangle p$ with the absolute time t at different conditions marked by lines of different colors: black line-2.0 mol/l brine was displaced by CO_2 with the rate of 0.05 ml/min in the 0.1 mm wide capillary duct, red line-the pure water was displaced by CO_2 with the rate of 0.01 ml/min in the 0.1 mm wide capillary duct, blue line-1.0 mol/l brine was displaced by CO_2 with the rate of 0.05 ml/min in the 0.1 mm wide capillary duct, orange line-1.5 mol/l brine was displaced by CO_2 with the rate of 0.05 ml/min in the 0.1 mm wide capillary duct, green line-the pure water was displaced by CO_2 with the rate of 0.01 ml/min in the 0.05 mm wide capillary

duct, purple line-the pure water was displaced by CO_2 with the rate of 0.05 ml/min in the 0.05 mm wide capillary duct.

The phenomenon of backflow mainly occurred in the second half of the duct where the capillary force dominated and it was mainly caused by the fluctuations of the pressure distributed along the two-phase interface (Bakhshian et al., 2019). Theoretically, the local velocity distribution transverse to the flow direction was symmetric, but the fluctuation caused by wettability triggered an imbalance of shear forces along the interface. Thus, this interface moved against the direction of injection until the forces rebalanced (Jiamin Wan, 1996). The pressure built up again to overcome the flow resistance and achieve the breakthrough. As shown in Fig. 18, the differential pressure $\triangle p$ would gradually drop to a value when the backflow occurred, and then an abrupt increase would cause Haines jump to achieve the breakthrough.

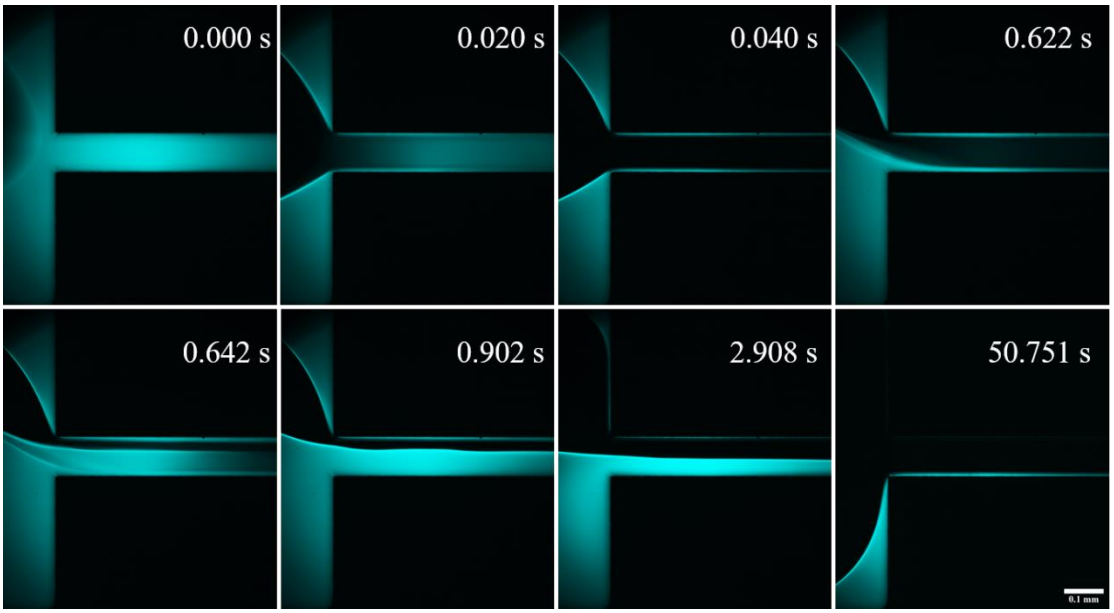

Figure 19. The more intense Haines jump in the 0.1 mm wide capillary duct when 2.0 mol/l brine was displaced by CO_2 at the rate of 0.05 ml/min. The camera's fps is 100. The injection direction is from left to right. Cyan represents the brine and black represents the CO_2 and micromodel skeleton.

In addition, the phenomenon of more intense Haines jump was found in this study, as shown in Fig. 19. The brine with the salinity of 2.0 mol/l was quickly displaced by CO_2 at the injection rate of 0.05 ml/min in 0.04 s, and it was consistent with the result simulated by Tsuji et al.(Tsuji et al., 2015) when the displacement pattern was crossover. In this study, this transient process could not be captured due to the limitation of camera's fps (repeated three times with fps of 50, 80, 100, respectively). There was an abrupt change of differential pressure to characterize this type of Haines jump, as shown in Fig. 18. After this happened, the residual aqueous phase near the entrance would enter the duct again during 0.622-0.902 s, as shown in Fig. 19. The brine

continued to enter the duct through the film to cause the film thickness to increase, and even tended to completely occupy the duct again. Due to the continuous injection of CO_2 and the limited amount of residual brine, finally, the aqueous phase in the duct was almost completely displaced. This phenomenon cannot be explained by the obtained pressure field in this study and needs to be further investigated.

4.2 The flow in the pore doublet model

Although the fields of velocity and pressure in the pore doublet model are more complex, the two-phase flow in the pore doublet model is easy to understand by analogy with the capillary duct. Theoretically, in the homogeneous pore doublet model, all three pressures are equal in the two ducts with the same width, and CO_2 can displace the water at the same velocity in both ducts, and finally two-phase interfaces meet at the exit to achieve the breakthrough (Chatzis and Dullien, 1983). In the heterogeneous pore doublet model, the total pressure drop required to initiate the displacement in the narrower duct is greater than the other duct due to the greater capillary force. Therefore, as CO_2 is injected, the total pressure drop rises to reach the critical pressure in the wider duct firstly, where the displacement occurs and breakthrough can be achieved. And since the total pressure drop cannot reach the critical pressure in the narrower duct, the brine will not be displaced and will remain in that duct. Most of the experimental results are in accordance with the theoretical analysis, but some experimental results deviate from theoretical analysis for the displacement at lower flow rate in homogeneous pore doublet model and higher flow rate in heterogeneous pore doublet model, as shown in Figures 20 and 21.

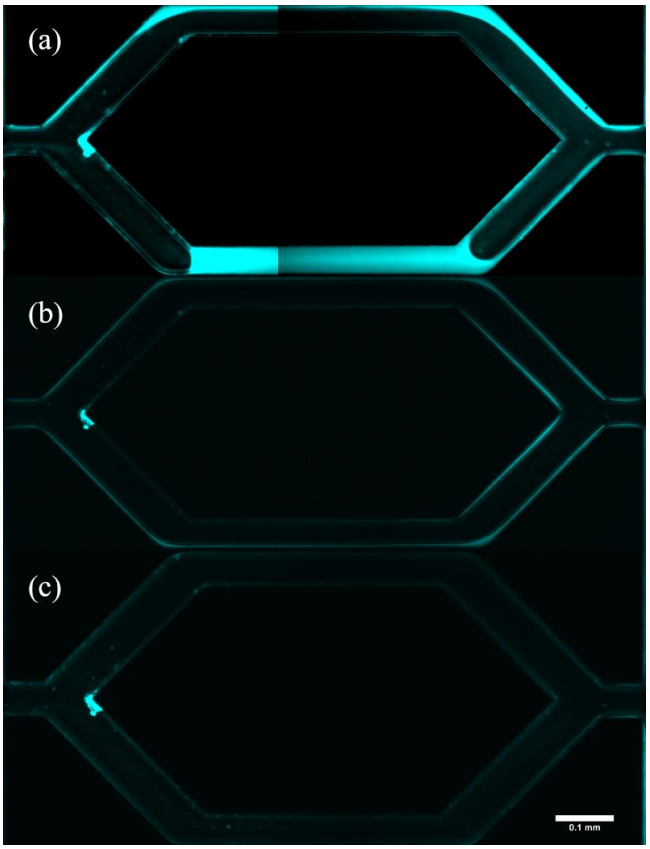

Figure 20. Images of CO_2 and water distributions at the quasi-steady state in the homogeneous pore doublet model at different injection rates: (a) 0.01 ml/min, (b) 0.05 ml/min, (c) 0.1 ml/min. The injection direction is from left to right. Cyan represents the brine and black represents the CO_2 and micromodel skeleton.

In the homogeneous pore doublet model, when the injection rate was 0.01 ml/min, the brine in the upper duct was completely displaced, while only the brine near the entrance and exit of the lower duct was displaced, and the residual brine was stabilized between the corners of the lower duct, as shown in Fig. 20(a). This was related to the dominance of capillary force at lower rate. Although two ducts had the same widths, the critical pressures needed to be overcome were different due to the wettability fluctuation caused by the roughness of the micromodel, so the displacement would preferentially occur in the duct with the lower critical breakthrough pressure. In addition, the corners in the model had an important effect on the two-phase flow. As can be seen in Fig. 20, there was an accumulation of aqueous phase and fluorescent dye at the corner of the duct bifurcation. At lower injection rate (0.01 ml/min in this study), not only the water in the lower duct was trapped between the corners, but a certain amount of water was captured at the corners of the upper duct. And the calculated residual saturation of water was 31.85%. The corner flow was more pronounced in the heterogeneous pore doublet model, as shown in Fig. 21.

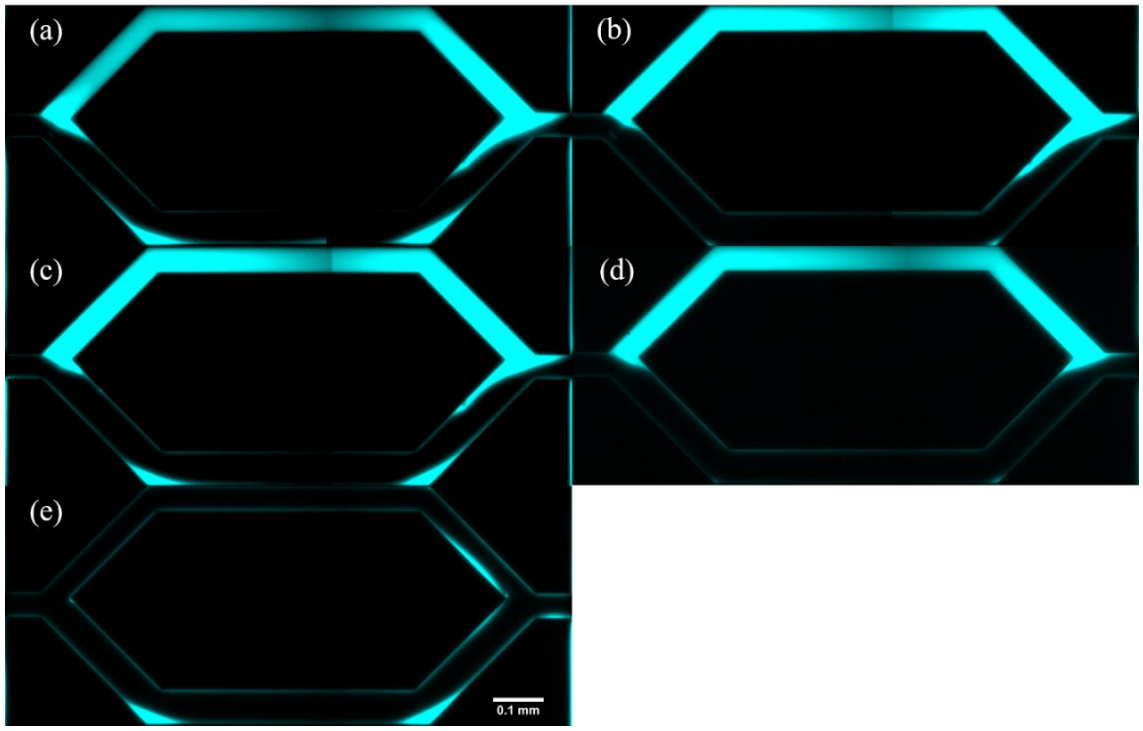

Figure 21. Images of CO_2 and water distributions at the quasi-steady state in the heterogeneous pore doublet model at different injection rates: (a) 0.002 ml/min, (b) 0.005 ml/min, (c) 0.01 ml/min, (d) 0.05 ml/min, (e) 0.1 ml/min. The injection direction is from left to right. Cyan represents the brine and black represents the CO_2 and micromodel skeleton.

The experimental results obtained in the heterogeneous pore doublet model were basically in agreement with the theoretical analysis (Chatzis and Dullien, 1983), as shown in Fig. 21. The water in the wider duct was completely displaced, while the displacement cannot occur in the narrower duct. Unlike the homogeneous pore doublet model, the residual wetting phase is distributed between the entrance and exit of the model, rather than between the corners of the narrower duct. The residual water saturations after the breakthrough were 61.01%, 48.42%, 55.50% and 46.11% when CO_2 was injected with the rates of 0.002, 0.005, 0.01 and 0.05 ml/min, respectively. And the fluctuation of saturation was mainly caused by the corner flow.

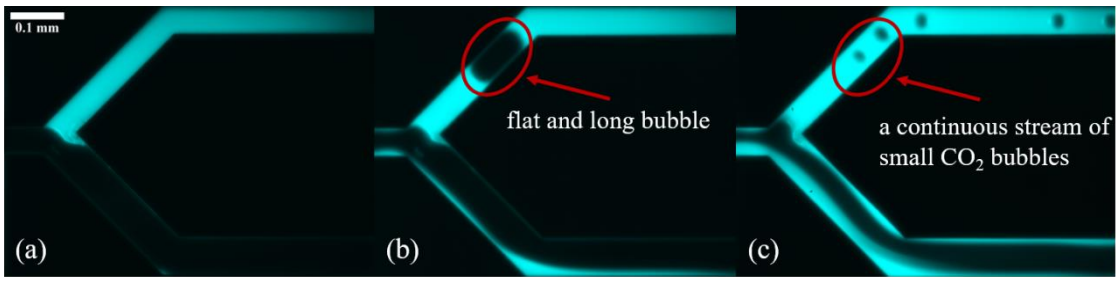

Figure 22. Different mechanisms of trapping water displaced by different forms of CO2 in the heterogeneous pore doublet model at different injection rates: (a) 0.002 ml/min, (b) 0.005 ml/min, (c) 0.05 ml/min. The injection direction is from left to right. Cyan represents the brine and black represents the CO2 and micromodel skeleton.

When CO_2 injection rate was 0.002 ml/min, the water in the narrower duct was never displaced by CO_2, and this low injection rate also caused the significant corner stagnation of water in wider duct, as shown in Figures 21(a) and 22(a). As the injection rate increased, although the water in narrower duct was not displaced after the breakthrough, CO_2 could enter this duct during the displacement process. When the CO_2 injection flow rate was 0.005 ml/min, CO_2 would enter the narrower duct in the form of flat and long bubbles after the breakthrough in the wider duct, as shown in Fig. 22(b). However, this form of CO_2 was unable to displace the brine and kept advancing in the aqueous phase to reach the outlet. When the stabilization pressure was reached, no more CO_2 bubbles would be produced. When the injection rate continued to increase to 0.1 ml/min, a continuous stream of small CO_2 bubbles would form to enter the narrower duct after the breakthrough in the wider duct, as shown in Fig. 22(c). Macroscopically, the brine could not be displaced as well by the form of continuous stream of CO_2 bubbles. Similarly, the CO_2 in bubble form would disappear when the stabilization pressure was reached, and then the final two-phase distribution was obtained. At high injection flow rate of 0.1 ml/min, the viscous force of water dominated, and the overall pressure drop at the inlet was large enough to satisfy the critical pressures required in two ducts with different widths at the same time. So, the displacement would occur to achieve the complete CO_2 saturation in both ducts simultaneously, as shown in Fig. 21(e). This is instructive for the storage capacity when CO_2 is injected into the brine aquifer.

5 Conclusions

CO_2 sequestration into the brine aquifer was researched in this study by conducting displacement experiments of CO_2/brine in four micromodels. The effects of the structure of micromodel, the injection rate of CO_2 and the salinity of brine on the two-phase flow were investigated. The parameters such as the differential pressure, contact angle, permeability, velocity field and force field were obtained using the microscopic visualization technique and image processing methods to discuss the displacement behavior in the capillary duct or pore doublet model.

Three important characteristic parameters: breakthrough time, critical pressure and stabilization pressure were summarized by analyzing the differential pressure. The materials used in this study were strongly hydrophilic through the measurement of advancing contact angle, which increased with increasing injection flow rate and decreasing salinity. CO_2 relative permeability increased with the injection rate and this relationship was stronger in the narrower duct. Conversely, the increase in the width of capillary duct and the number of ducts would decrease CO_2 relative permeability. The effect of salinity on CO_2 relative permeability was more complex due to the salting out. The local velocity was about 3 orders of magnitude smaller than the bulk injection velocity, and the velocity field was affected by the displacement pattern. The force field in the capillary duct proved that the displacement pattern was not constant during the flow.

These characteristic parameters were combined to analyze the two-phase flow in the capillary duct and pore doublet model. The backflow of brine was observed when it was displaced by CO_2 at the rate of 0.01 and 0.05 ml/min and the more tense Haines jump was found in the 0.1 mm wide duct when 2.0 mol/l brine was displaced by CO_2 at 0.05 ml/min injection rate. In the homogeneous pore doublet model, the water could be completely displaced in both ducts, and when the injection rate decreased, part of the water would be trapped. In the heterogeneous pore doublet model, the water was completely displaced only in the wider duct, while the water in the narrower duct was trapped at lower injection flow rate through different trapping mechanisms: completely non-displaced, flat and long bubbles, continuous stream of small bubbles. However, the water in two ducts could be completely displaced in the heterogenous pore doublet model at higher injection rate.

Acknowledgments

This work was supported by the National Natural Science Foundation of China (Grant 51976024), LiaoNing Revitalization Talents Program (Grant XLYC2007117) and the Fundamental Research Funds for the Central Universities (Grant DUT21LAB104).

References

NIST, edited, http://webbook.nist.gov/chemistry/fluid/.

Bachu, S., and B. Bennion (2008), Effects of in-situ conditions on relative permeability characteristics of CO_2-brine systems, Environmental Geology, 54(8), 1707-1722.

727 Bai, M., L. Liu, C. Li, and K. Song (2020), Relative Permeability Characteristics During Carbon
728 Capture and Sequestration Process in Low-Permeable Reservoirs, Materials (Basel), 13(4).
729 Bakhshian, S., S. A. Hosseini, and N. Shokri (2019), Pore-scale characteristics of multiphase flow
730 in heterogeneous porous media using the lattice Boltzmann method, Sci Rep, 9(1), 3377.
731 Berejnov, V., N. Djilali, and D. Sinton (2008), Lab-on-chip methodologies for the study of
732 transport in porous media: energy applications, Lab Chip, 8(5), 689-693.
733 Chang, C., Q. Zhou, J. Guo, and Q. Yu (2014), Supercritical CO_2 dissolution and mass transfer in
734 low-permeability sandstone: Effect of concentration difference in water-flood experiments,
735 International Journal of Greenhouse Gas Control, 28, 328-342.
736 Chang, C., Q. Zhou, M. Oostrom, T. J. Kneafsey, and H. Mehta (2017), Pore-scale supercritical
737 CO_2 dissolution and mass transfer under drainage conditions, Advances in Water Resources, 100,
738 14-25.
739 Chang, C., T. J. Kneafsey, Q. Zhou, M. Oostrom, and Y. Ju (2019), Scaling the impacts of pore-
740 scale characteristics on unstable supercritical CO_2-water drainage using a complete capillary
741 number, International Journal of Greenhouse Gas Control, 86, 11-21.
742 Chang, C., T. J. Kneafsey, J. Wan, T. K. Tokunaga, and S. Nakagawa (2020), Impacts of Mixed-
743 Wettability on Brine Drainage and Supercritical CO_2 Storage Efficiency in a 2.5-D Heterogeneous
744 Micromodel, Water Resources Research, 56(7).
745 Chang, C., Q. Zhou, T. J. Kneafsey, M. Oostrom, T. W. Wietsma, and Q. Yu (2016), Pore-scale
746 supercritical CO_2 dissolution and mass transfer under imbibition conditions, Advances in Water
747 Resources, 92, 142-158.
748 Chatzis, I., and F. Dullien (1983), Dynamic immiscible displacement mechanisms in pore
749 doublets: Theory versus experiment, Journal of Colloid & Interface Science, 91(1), 199-222.

Chen, X., A. Kianinejad, and D. A. DiCarlo (2016), An extended JBN method of determining unsteady-state two-phase relative permeability, Water Resources Research, 52(10), 8374-8383.

Gaol, C. L., J. Wegner, and L. Ganzer (2020), Real structure micromodels based on reservoir rocks for enhanced oil recovery (EOR) applications, Lab Chip.

Huang Daming, T. Z., Ge Chuanding, Wang Yuying, Sun Chuanmei (1984), Gas-water relative permeability of low permeability cores measured by stabilization method, Natural Gas Industry, 4(2), 25-30.

Jafari, M., and J. Jung (2017), Direct Measurement of Static and Dynamic Contact Angles Using a Random Micromodel Considering Geological CO_2 Sequestration, Sustainability, 9(12), 2352.

Jafari, M., and J. Jung (2019), Salinity effect on micro-scale contact angles using a 2D micromodel for geological carbon dioxide sequestration, Journal of Petroleum Science and Engineering, 178, 152-161.

Jiamin Wan, T. K. T., Chin-Fu Tsang, and Gudmundur S. Bodvarsson (1996), Improved Glass Micromodel Methods for Studies of Flow and Transport in Fractured Porous Media, Water Resources Research, 32(7), 1955-1964.

Jin, X., C. Chao, K. Wu, C. Xia, and X. Fan (2020), The effect of CO_2 phase on drainage process by analysis of transient differential pressure, Chemical Engineering Science, 218, 115581.

Juanes, R. (2006), Impact of relative permeability hysteresis on geological CO_2 storage, Water Resources Research, 42(12).

Juncker, D., H. Schmid, U. Drechsler, H. Wolf, M. Wolf, B. Michel, N. de Rooij, and E. Delamarche (2002), Autonomous Microfluidic Capillary System, Analytical Chemistry, 74(24), 6139-6144.

772 Kazemifar, F., G. Blois, D. C. Kyritsis, and K. T. Christensen (2015), A methodology for velocity
773 field measurement in multiphase high-pressure flow of CO_2 and water in micromodels, Water
774 Resources Research, 51(4), 3017.
775 Kazemifar, F., G. Blois, D. C. Kyritsis, and K. T. Christensen (2016), Quantifying the flow
776 dynamics of supercritical CO_2-water displacement in a 2D porous micromodel using fluorescent
777 microscopy and microscopic PIV, Advances in Water Resources, 95, 352-368.
778 Lenormand, R., and C. Zarcone (1985), Invasion percolation in an etched network: Measurement
779 of a fractal dimension, Phys Rev Lett, 54(20), 2226-2229.
780 Lenormand, R., C. Zarcone, and A. Sarr (1983), Mechanisms of the displacement of one fluid by
781 another in a network of capillary ducts, Journal of Fluid Mechanics, 135(135), 337-353.
782 Lenormand, R., E. Touboul, and C. Zarcone (1987), Numerical models and experiments on
783 immiscible displacements in porous media, Journal of Fluid Mechanics, 189(-1), 165.
784 Li, Z., S. Wang, S. Li, W. Liu, B. Li, and Q.-C. Lv (2013), Accurate Determination of the CO_2-
785 Brine Interfacial Tension Using Graphical Alternating Conditional Expectation, Energy & Fuels,
786 28(1), 624-635.
787 M. Dong, I. C. (1995), The imbibition and flow of a wetting liquid along the corners of a square
788 capillary tube, Journal of Colloid and Interface Science, 172, 278-288.
789 Mao, S., and Z. Duan (2009), The Viscosity of Aqueous Alkali-Chloride Solutions up to 623 K,
790 1,000 bar, and High Ionic Strength, International Journal of Thermophysics, 30(5), 1510-1523.
791 Morais, S., N. Liu, A. Diouf, D. Bernard, C. Lecoutre, Y. Garrabos, and S. Marre (2016),
792 Monitoring CO_2 invasion processes at the pore scale using geological labs on chip, Lab Chip,
793 16(18), 3493-3502.

794 Mortensen, N. A., F. Okkels, and H. Bruus (2005), Reexamination of Hagen-Poiseuille flow: shape
795 dependence of the hydraulic resistance in microchannels, Phys Rev E Stat Nonlin Soft Matter
796 Phys, 71(5 Pt 2), 057301.
797 Patmonoaji, A., M. Muharrik, Y. Hu, C. Zhang, and T. Suekane (2020), Three-dimensional
798 fingering structures in immiscible flow at the crossover from viscous to capillary fingering,
799 International Journal of Multiphase Flow, 122, 103147.
800 Sell, A., H. Fadaei, M. Kim, and D. Sinton (2013), Measurement of CO_2 diffusivity for carbon
801 sequestration: a microfluidic approach for reservoir-specific analysis, Environ Sci Technol, 47(1),
802 71-78.
803 Song, Y., C. Zhao, M. Chen, Y. Chi, Y. Zhang, and J. Zhao (2020), Pore-scale visualization study
804 on CO_2 displacement of brine in micromodels with circular and square cross sections, International
805 Journal of Greenhouse Gas Control, 95.
806 Tsuji, Takeshi, Matsuoka, Toshifumi, Yamabe, Hirotatsu, Liang, and Yunfeng (2015), Lattice
807 Boltzmann Simulations of Supercritical CO_2-Water Drainage Displacement in Porous Media: CO_2
808 Saturation and Displacement Mechanism, Environmental Science & Technology: ES&T, 49(1),
809 537-543.
810 Werth, C. J., C. Zhang, M. L. Brusseau, M. Oostrom, and T. Baumann (2010), A review of non-
811 invasive imaging methods and applications in contaminant hydrogeology research, J Contam
812 Hydrol, 113(1-4), 1-24.
813 Wu, M., F. Xiao, R. M. Johnson-Paben, S. T. Retterer, X. Yin, and K. B. Neeves (2012), Single-
814 and two-phase flow in microfluidic porous media analogs based on Voronoi tessellation, Lab Chip,
815 12(2), 253-261.

816 Zhang, C., M. Oostrom, T. W. Wietsma, J. W. Grate, and M. G. Warner (2011), Influence of
817 Viscous and Capillary Forces on Immiscible Fluid Displacement: Pore-Scale Experimental Study
818 in a Water-Wet Micromodel Demonstrating Viscous and Capillary Fingering, Energy & Fuels,
819 25(8), 3493-3505.
820 Zhu, Y., and K. Petkovic-Duran (2009), Capillary flow in microchannels, Microfluidics and
821 Nanofluidics, 8(2), 275-282.
822